PCCP
Physical Chemistry Chemical Physics

# Accepted Manuscript

This article can be cited before page numbers have been issued, to do this please use: K. Arima, Y. Kodani, M. Hotta and N. Koga, *Phys. Chem. Chem. Phys.*, 2026, DOI: 10.1039/D6CP00975A.




ROYAL SOCIETY OF CHEMISTRY

rsc.li/pccp

View Article Online
DOI: 10.1039/D6CP00975A

# Multistep Kinetics of the Thermal Decomposition of β-Nickel Hydroxide: Extraction of the Primary Reaction Steps and the Effect of Water Vapor Pressure

Kazuki Arima, Yuna Kodani, Mito Hotta, and Nobuyoshi Koga*

Department of Science Education, Graduate School of Humanities and Social Sciences, Hiroshima University, 1-1-1 Kagamiyama, Higashi-Hiroshima 739-8524, Japan



## Abstract

The thermal decomposition of nickel hydroxide ($Ni(OH)_2$) was investigated using thermoanalytical techniques with specific focuses on the multistep kinetic behavior and the effect of the partial pressure of water vapor ($p(H_2O)$). The thermal decomposition process was modeled as a four-step kinetic process, comprising the dehydration of absorbed or included water, two-step primary reaction process yielding nickel oxide (NiO), and the evolution of the trapped water molecules as the crystal growth of NiO progressed. The kinetic characteristics of the individual reaction steps in the primary reaction process were revealed using advanced kinetic analysis methodologies for multistep reactions. A distinctive retardation effect of atmospheric water vapor pressure ($p(H_2O)_{ATM}$) was evidenced by systematically tracing the reaction process at varying $p(H_2O)_{ATM}$ values. Combining the kinetic analysis methodologies for multistep reactions and universal kinetic description across different $p(H_2O)$ values, the individual reaction steps in the primary reaction process were described as a function of temperature, degree of reaction, and $p(H_2O)_{ATM}$. This approach was further extended to incorporate the effect of the self-generated water vapor pressure, thereby enabling the universal kinetic description covering all kinetic data in a stream of dry and wet $N_2$ gases. The kinetic results indicated the initial reaction step in the primary reaction process as being regulative of the primary reaction process in the context of the physico-geometrical kinetic behavior and the effect of $p(H_2O)$. The novel kinetic findings are expected to serve as the necessary information to refine the thermal processing of $Ni(OH)_2$, yielding NiO with the desired properties and morphologies.

Keywords: Nickel hydroxide, Thermal decomposition, Multistep kinetics, Water vapor effect, Nickel oxide

## 1. Introduction

Nickel hydroxide ($Ni(OH)_2$) have a variety of applications in modern battery technology.[1] The diverse functional properties of this material have significant implications for research in synthesis and characterization. This material is also a precursor to nickel oxide (NiO), which have a variety of applications, including as photocatalysts, gas sensors, electrochromics, and supercapacitors.[2-8] Novel physical, chemical, and bio-inspired green mediated processes have been developed for the synthesis of nano-sized and nano-morphological $Ni(OH)_2$ and NiO with enhanced functionalities.[1, 9-12] The preparation of NiO via the thermal decomposition of nickel

compounds is a well-established method. However, it can also be regarded as innovative when the high reactive precursor with preferable size and morphology is synthesized and the thermal decomposition process is meticulously controlled. It is also noteworthy that the formation of a nickel compound and its thermal decomposition process are relevant component processes in the other modern synthetic techniques. Nevertheless, the regulation of thermal decomposition process poses significant empirical challenges in numerous synthetic techniques, necessitating the selection of optimal processing conditions through a process of trial and error, which is generally observed for a range of metal oxide processing techniques.[13] Therefore, the kinetic characterization of the thermal decomposition process of the precursor materials poses a continuous challenge to gain further insight into the reaction process controlled by complex physico-geometrical constraints. Furthermore, it is necessary to obtain the relevant information to control the reaction process in order to obtain metal oxides with specific properties for practical applications.

The thermal decomposition of $Ni(OH)_2$ with a variety of morphological characteristics has been studied in views of the variations in the reaction behavior and the morphology of the solid product, NiO.[14-21]

$$Ni(OH)_2(s) \rightarrow NiO(s) + H_2O(g) \quad (1)$$

The multistep mass loss behavior has been observed for $Ni(OH)_2$ samples with different morphological characteristics when it was heated under linearly increasing temperature conditions.[14-21] The reaction initiates with a slow mass loss rate, which abruptly transitions to a rapid mass loss stage that exhibits the major mass loss value within a limited temperature range. This is followed by a gradual mass loss process continuing to higher temperatures. The kinetic analysis of the overall process was performed using classical calculation methods for the reactions under isothermal and linearly increasing temperature conditions,[14, 19, 22, 23] without considering the multistep thermal decomposition behavior. The multistep thermal behavior of the thermal decomposition of $Ni(OH)_2$ was clearly traced by a specific thermoanalytical method of constant transformation rate thermal analysis (CRTA),[20] which is a technique of sample controlled thermal analysis.[24] Logvinenko et al. presented a multistep kinetic analysis for the thermal decomposition of $Ni(OH)_2$ using a commercially available kinetic analysis software.[18] The recent advancements of the kinetic analysis for the multistep reaction processes are expected to offer further insights into multistep kinetic behavior and reveal the physicochemical and physico-geometrical characteristics of the individual component reaction steps.[25, 26]

Another concern regarding the kinetics of the thermal decomposition of $Ni(OH)_2$ pertains to the effect of the partial pressure of water vapor ($p(H_2O)$), which is involved in the reaction atmosphere ($p(H_2O)_{ATM}$) and is self-generated by the reaction ($p(H_2O)_{SG}$), on the kinetic behavior of the reaction. To the best of our knowledge, available information on the subject for the thermal decomposition of $Ni(OH)_2$ is limited. The effect of $p(H_2O)$ on the kinetics is unavoidable, particularly in the context of reversible thermal dehydration/dehydroxylation processes.[27] Recently, we reported the distinctive retardation effect of $p(H_2O)$ on the thermal decomposition of $Ca(OH)_2$, $Mg(OH)_2$, and $Cu(OH)_2$.[28-30] The analogous effect of the gaseous species of the product in the reaction atmosphere has been observed for the thermal dehydration of inorganic hydrates[31-36] and metal carbonates.[33, 37, 38] Besides, the thermal decomposition of $Zn(OH)_2$ exhibited no distinguishable changes in the kinetic behavior in response to the variation in $p(H_2O)_{ATM}$.[39] Therefore, a systematic investigation into the effect of $p(H_2O)$ on the thermal decomposition of $Ni(OH)_2$ is imperative to elucidate the kinetic characteristics. Furthermore, the universal kinetic description of the reversible thermal dehydration and dehydroxylation processes as a function of temperature ($T$), degree of reaction

($\alpha$), and $p(H_2O)$ can be recognized as one of the most distinguishable recent achievements in the field of the kinetics of the thermal decomposition of solids.[40, 41] Such advanced kinetic description is expected to be applicable to the thermal decomposition of $Ni(OH)_2$, thereby unveiling hitherto unexplored aspects of the kinetics.

This study demonstrates an advanced kinetic approach to the thermal decomposition of $Ni(OH)_2$ to form NiO, utilizing state-of-the-art methodologies, namely kinetic analysis for the multistep process and universal kinetic description as a function of $T$, $\alpha$, and $p(H_2O)$. The objective of this study was to reveal the physicochemical and physico-geometrical characteristics of each component reaction step in the multistep reaction, based on the outcomes of these advanced kinetic approaches. Furthermore, it elucidates the effect of $p(H_2O)$ on each reaction step, providing a universal kinetic description of the primary thermal decomposition process in the multistep reaction across a range of $T$ and $p(H_2O)$ values. The novel physicochemical findings of the kinetic are expected to contribute to a further sophisticated control of the thermal decomposition process of $Ni(OH)_2$, resulting in the formation of the NiO with desired physical properties and morphologies.

## 2. Experimental

### 2.1 Sample preparation and characterization

A stock solutions of 0.5 M-$Ni(NO_3)_2$(aq) and 1.0 M-KOH(aq) were prepared by dissolving $Ni(NO_3)_2 \cdot 6H_2O$ (special grade, Sigma-Aldrich Japan) and KOH (special grade, Kishida Chem.) into deionized and distilled water, respectively. In a similar manner, a solution of 10 wt%-$NH_3$(aq) was prepared by diluting 25%-$NH_3$(aq) (special grade, FUJIFILM Wako). A 100 $cm^3$ of 0.5 M-$Ni(NO_3)_2$ was dropwise titrated with 70 $cm^3$ of 10%-$NH_3$(aq) to obtain a solution of $[Ni(NH_3)_4](NO_3)_2$(aq). The ammonia complex solution of $Ni^{2+}$ was maintained at approximately 323 K, and a total of 100 $cm^3$ of 1.0 M-KOH(aq) was titrated at a rate of 2 $cm^3$ $min^{-1}$. During the titration process, the solution was subjected to mechanical stirring. The precipitate resulting from the KOH(aq) titration was filtered and subsequently washed repeatedly with deionized and distilled water. The separated precipitate was then dried at 323 K for 24 h in an ambient air atmosphere using an electric oven (DK240S, Yamato). Thereafter, the desiccated precipitate was pulverized using an agate mortar and pestle, and used as the sample for this study. It is acknowledged that, in preparation for the present study, a series of $Ni(OH)_2$ and basic nickel salts were prepared by systematically varying mother liquors and precipitation conditions. The $Ni(OH)_2$ sample prepared utilizing the aforementioned method was selected on the basis of its elevated degree of crystallinity and minimal absorbed water content, in order to facilitate the thermoanalytical tracking of the primary stage of the thermal decomposition process. According to the findings of Ramesh et al.,[42, 43] $Ni(OH)_2$ with elevated crystallinity has been observed to precipitate within the pH range of ammonia solutions, as observed in this study.

The sample was characterized using powder X-ray diffractometry (XRD) and Fourier transform infrared spectroscopy (FTIR). The sample was press-fitted onto a sample holder plate and subsequently subjected to XRD measurement using a diffractometer (RINT-2200V, Rigaku). The XRD pattern was measured by irradiating Cu-$K_\alpha$ (40 kV, 20 mA) and scanning $2\theta$ value from 5° to 60° at a scan speed of 4° $min^{-1}$ in steps of 0.02°. For the FTIR measurement, the sample was diluted with KBr through grinding with an agate mortar and pestle, and the IR spectrum was recorded using a spectrometer (FT-IR 8600, Shimadzu) employing the diffuse reflectance method. For the morphological characterization, surface textures of the sample particles were observed using a scanning electron microscope (SEM, JSM-6510, JEOL) after the sample was coated with a thin Pt layer by sputtering (JFC-

View Article Online
DOI: 10.1039/D6CP00975A

1600, JEOL, 30 mA, 30 s). The specific surface area ($S_{BET}$) was determined by the Brunauer–Emmett–Teller (BET) single point method using a Flow Sorb II 2300 instrument (Micromeritics). The particle size distribution (PSD) was analyzed using an instrument (SALD-300 V, Shimadzu) via a laser diffraction method.

2.2 Thermal behavior

The thermal behavior of the $Ni(OH)_2$ sample was traced using simultaneous thermogravimetry (TG)–differential thermal analysis (DTA) coupled with a mass spectroscopy (MS) for the evolved gas (TG/DTA–MS) and high temperature XRD (HTXRD). The TG/DTA–MS measurements were conducted with an instrument constructed using a TG–DTA (TG8120, Rigaku) and MS (M200-QA, Anelva), which were connected via a transfer line of the evolved gas. The 5.0 mg sample was weighed into a Pt sample pan (5 mm in diameter and 2.5 mm in depth). The TG–DTA measurement was carried out by heating the sample from 300 to 873 K at a $\beta$ of 5 K $min^{-1}$ in a stream of helium at a flow rate ($q_v$) of 200 $cm^3$ $min^{-1}$. During the TG–DTA measurement, a portion of the outlet gas was continuously transferred to the MS via a silica capillary tube (inner diameter: 75 μm; length: 750 mm) that have been heated at 573 K. The MS measurements were then repeated in a range of $m/z$ 10–50 by electron impact mode (70 eV) with the secondary electron multiplier (SEM; 1.0 mA, 1.0 kV).

For the XRD measurement, the sample was press-fitted to a Pt sample holder plate and the XRD patterns were recorded using the RINT-2200V diffractometer by additionally equipping with a programable heating chamber. The sample was heated according to two distinct temperature programs in a stream of dry $N_2$ ($q_v$ = 100 $cm^3$ $min^{-1}$). The XRD measurements were performed at various programmed temperatures or times during the execution of these heating programs. In the stepwise isothermal heating mode, the sample was heated at a heating rate ($\beta$) of 5 K $min^{-1}$ from room temperature to 773 K, during which isothermal holding sections for each 15 min were inserted every 25 K in a temperature range from 323 to 773 K. The XRD patterns were recorded during each isothermal holding section. In the isothermal heating mode, the sample was heated to 523 K at a $\beta$ of 10 K $min^{-1}$ and maintained at that temperature for 10 h. During the isothermal holding section, diffraction measurements were repeated for a total of 40 times. The XRD measurement conditions were identical to those at room temperature for sample characterization described above.

Approximately 300 mg of the $Ni(OH)_2$ sample was weighed into an alumina boat (SSA-S #6A, length: 100 mm, width: 14 mm, height: 10 mm). Using an electric tube furnace, the sample was heated to various temperatures in a range of 448–773 K at a $\beta$ of 5 K $min^{-1}$ in a stream of dry $N_2$ at a $q_v$ of 100 $cm^3$ $min^{-1}$. The heat-treated sample was recovered after cooling to room temperature in the tube furnace, and subsequently subjected to the measurement of $S_{BET}$.

2.3 Tracking of thermal decomposition process in a stream of dry $N_2$

The thermal decomposition process of the $Ni(OH)_2$ sample in a stream of dry $N_2$ was tracked using a simultaneous TG–DTA (STA7300, Hitachi High Tech.). Before the measurement of a series of TG–DTA curves for the kinetic calculation, test runs were conducted to select appropriate measurement conditions including sample mass ($m_0$) and the $q_v$ value of dry $N_2$. The sample of varying $m_0$ values ($1.0 \leq m_0/mg \leq 10.0$) was weighed in a Pt pan (diameter: 5.0 mm; depth: 2.5 mm), and TG–DTA measurements were carried out during the heating of the sample from 300 to 873 K at a $\beta$ of 5 K $min^{-1}$ in a stream of dry $N_2$ ($q_v$ = 300 $cm^3$ $min^{-1}$). In an alternative series of

View Article Online
DOI: 10.1039/D6CP00975A

TG–DTA measurements, the $m_0$ value was fixed to be 5.00 ± 0.05 mg and the sample was heated from 300 to 873 K at a $\beta$ of 5 K min$^{-1}$ in a stream of dry $N_2$ with varying $q_v$ values ($50 \leq q_v/\text{cm}^3\ \text{min}^{-1} \leq 500$).

Based on the results of the preliminary TG–DTA measurements, the $m_0$ and $q_v$ values for the TG–DTA measurement to obtain the kinetic data were fixed to be 5.00 ± 0.05 mg and 300 cm$^3$ min$^{-1}$, respectively. The TG–DTA measurements were conducted under three different heating program modes including linear nonisothermal, isothermal, and stepwise isothermal modes, in which the stepwise isothermal mode is categorized into the sample controlled thermal analysis technique.[24, 44] For the TG–DTA measurements under linear nonisothermal conditions, the sample was heated from 300 to 873 K at varying $\beta$ values ($0.5 \leq \beta/\text{K min}^{-1} \leq 10$). The TG–DTA measurements under isothermal conditions were conducted by linearly heating the sample from 300 K to different preset temperatures ($479 \leq T/\text{K} \leq 507$) at a $\beta$ of 10 K min$^{-1}$ and maintained at the temperature until the mass loss process was completed. In the measurement of the stepwise isothermal mode, the sample was basically heated from 300 to 873 K at a $\beta$ of 2 K min$^{-1}$, whereas, when the mass loss rate reached to the programmed threshold value ($C$), temperature program mode was switched to isothermal mode. The opposite was applied when the mass loss rate was reduced to the $C$ value during the isothermal section, switching to the linear nonisothermal mode at a $\beta$ of 2 K min$^{-1}$. The measurements in the stepwise isothermal model were conducted at varying $C$ values in a range of 5–20 μg min$^{-1}$. It is noteworthy that the repeatability of the TG–DTA curves was confirmed for the measurements at selected measurement conditions for each measurement under linear nonisothermal, isothermal, and stepwise isothermal modes. Furthermore, systematic shifts in the thermoanalytical curves with the heating parameters of $\beta$, $T$, and $C$ were investigated as an indicator of reproducibility.

In the course of the TG–DTA measurements of the $Ni(OH)_2$ sample ($m_0$ = 5.0 mg) under linear nonisothermal conditions at a $\beta$ of 5 K min$^{-1}$ in a stream of dry $N_2$ ($q_v$ = 300 cm$^3$ min$^{-1}$), the measurements were terminated at various temperatures in the temperature range of the mass loss process to obtain the partially decomposed sample at different $\alpha$ values. Subsequently, the heat-treated samples were subjected to SEM observations.

### 2.4 Tracking of thermal decomposition process in a stream of wet $N_2$

The thermal decomposition process of $Ni(OH)_2$ was also traced in a stream of wet $N_2$ characterized by different $p(H_2O)_{ATM}$ values using a humidity-controlled TG (HUM-TG) system, which was constructed with a TG–DTA (TG8120, Rigaku) and a humidity controller (HUM-1, Rigaku). The construction and operation of the HUM-TG system were detailed in some previous publications.[35, 36] Using the 5.0 mg sample weighed into a Pt pan (diameter: 5.0 mm; depth: 2.5 mm), a series of TG–DTA measurements was conducted in the linear nonisothermal mode at a fixed $\beta$ of 5 K min$^{-1}$ in a stream of wet $N_2$ ($q_v$ = 300–400 cm$^3$ min$^{-1}$) with varying $p(H_2O)_{ATM}$ values in a range of 0.8–10.2 kPa. Notably, the $q_v$ value of the wet $N_2$ flow was varied among the measurements depending on the controlled $p(H_2O)_{ATM}$ value of the wet $N_2$, in order to regulate the $p(H_2O)_{ATM}$ value by mixing a wet and dry $N_2$ flowing at different flow rates. Furthermore, by selecting three different $p(H_2O)_{ATM}$ values of 0.8, 3.6, and 9.2 kPa as a reaction condition, kinetic data under different temperature conditions were obtained by the TG–DTA measurements in the linear nonisothermal mode at varying $\beta$ values and the isothermal mode at varying preset temperatures at each $p(H_2O)_{ATM}$ values. In the linear nonisothermal mode, the sample was heated from 300 to 973 K at different $\beta$ values ($0.5 \leq \beta/\text{K min}^{-1} \leq 10$). In the isothermal mode, the sample was heated to different preset

temperatures at a $\beta$ of 10 K min$^{-1}$ and subsequently maintained at that temperature until the reaction was complete. The temperature range of the measurements in the isothermal mode was varied with the $p(H_2O)_{ATM}$ value, which was $504 \leq T/K \leq 523$, $512 \leq T/K \leq 532$, and $516 \leq T/K \leq 535$ for the measurements in a stream of wet $N_2$ with $p(H_2O)_{ATM}$ values of 0.8, 3.6, and 9.2 kPa, respectively.

## 3. Results and discussion

### 3.1 Sample characterization

Figure S1 shows the XRD pattern and FTIR spectrum of the sample. The XRD pattern was agreed with that of β-Ni(OH)$_2$ (hexagonal, S.G. = *P*-3*m*1(164), $a = b = 0.31300$ nm, $c = 0.46300$ nm, $\alpha = \beta = 90.000°$, $\gamma = 120.000°$, ICDD 01-074-2075).[45] The FTIR spectrum exhibited specific IR absorption peaks at 3639, 542, and 459 cm$^{-1}$, which are attributed to the O–H stretching of non-hydrogen bonded OH groups, an in-plane bending of Ni–O–H, and Ni–O stretching, respectively.[46, 47] Figure S2 shows the SEM image of the Ni(OH)$_2$ sample. The sample was characterized as an agglomerate of nano-micrometer sized particles with the $S_{BET}$ value of 28.0 ± 0.1 m$^2$ g$^{-1}$. The sample particles exhibited a size distribution (Figure S3), which was characterized by the average diameter size of 0.685 μm with the standard deviation of 0.274 in logarithmic scale along the log normal distribution function.

### 3.2 Thermal behavior

Figure 1 shows the results of TG/DTA–MS measurements. The TG curve demonstrated a modest mass loss below 400 K, a pronounced mass loss between 450 and 570 K, and a gradual mass loss extending to approximately 750 K. The primary mass loss process observed between 450–570 K was accompanied by a significant endothermic effect as observed in the DTA curve. Only the evolution of water vapor was detected by the peak of *m*/*z* 18 ($H_2O^+$) and its fragments in the MS thermograms during the entire temperature range of the TG/DTA–MS measurement.

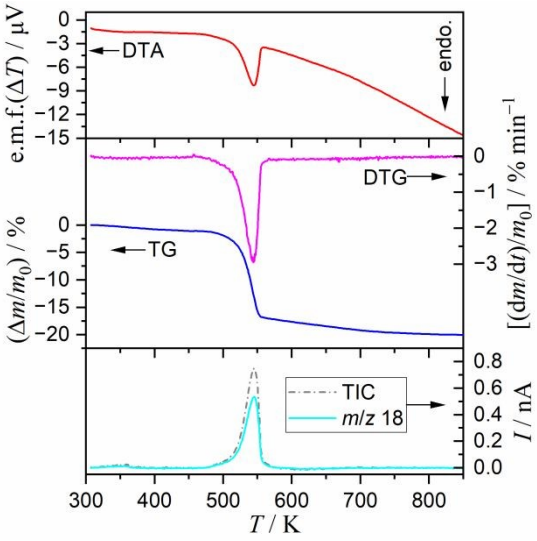


**Figure 1.** Results of TG/DTA–MS measurement for the thermal decomposition of Ni(OH)$_2$ ($m_0$ = 5.00 mg) at a $\beta$ of 5 K min$^{-1}$ in a stream of He at a $q_v$ of 200 cm$^3$ min$^{-1}$.

Figure 2 shows the results of HTXRD measurements during heating the sample in the stepwise isothermal

mode at a $\beta$ of 5 K min$^{-1}$ with isothermal holding sections at various temperatures in a stream of dry $N_2$ ($q_v$ = 100 cm$^3$ min$^{-1}$). The XRD pattern of the original sample was maintained up to 523 K (Figure 2(a)). Therefore, the initial mass loss observed below 400 K can be attributed to the dehydration of absorbed or included water in the original $Ni(OH)_2$ sample. The change in the XRD pattern was observed in the temperature range from 523 to 573 K, which covers the temperature range of the primary mass loss step of the thermal decomposition observed in TG. The product phase was identified as NiO (Figure 2(b); trigonal, S.G.: *R*-3*m*(166), $a = b = 0.29895$ nm, $c = 0.73210$ nm, $\alpha = \beta = 90.000°$, $\gamma = 120.000°$, ICDD 01-078-4383).[48] After the transformation, the intensity of the XRD peaks attributed to NiO increased gradually as the temperature increased from 573 to 773 K. This was accompanied by the gradual increase in the crystallite size of NiO during heating from 573 to 773 K (Figure 2(c)). It was thus anticipated that the gradual mass loss observed in the corresponding temperature range of the growth of XRD peaks of NiO can be attributed to the removal of the water molecules trapped in the NiO particles and these agglomerates. As illustrated in Figure S4, at a constant temperature of 523 K, the gradual attenuation of the XRD peaks of $Ni(OH)_2$ and compensative growth of the XRD peaks of NiO occurred without exhibiting any evidence of the formation of intermediate crystalline solids. The crystallite size of NiO obtained by the isothermal treatment for 600 min was calculated to be 3.2 nm using the Rietveld refinement analysis, which was slightly smaller than that calculated for the NiO at 548 K during the stepwise isothermal heating (Figure 2(c)). As illustrated in Figure S5, the $S_{BET}$ value of the sample exhibited a substantial increased to 146.0 m$^2$ g$^{-1}$ within the temperature range of the primary thermal decomposition process, i.e., 523–573 K, followed by a decline upon further heating to 773 K. However, the appearance of the sample particles as an agglomerate of nano particles remained relatively unchanged during the thermal decomposition process, as shown in Figure S6. The findings indicated that the primary mass loss process occurred within the temperature range from 523 to 573 K can be treated as the thermal decomposition process of $Ni(OH)_2$ to form NiO.



View Article Online
DOI: 10.1039/D6CP00975A



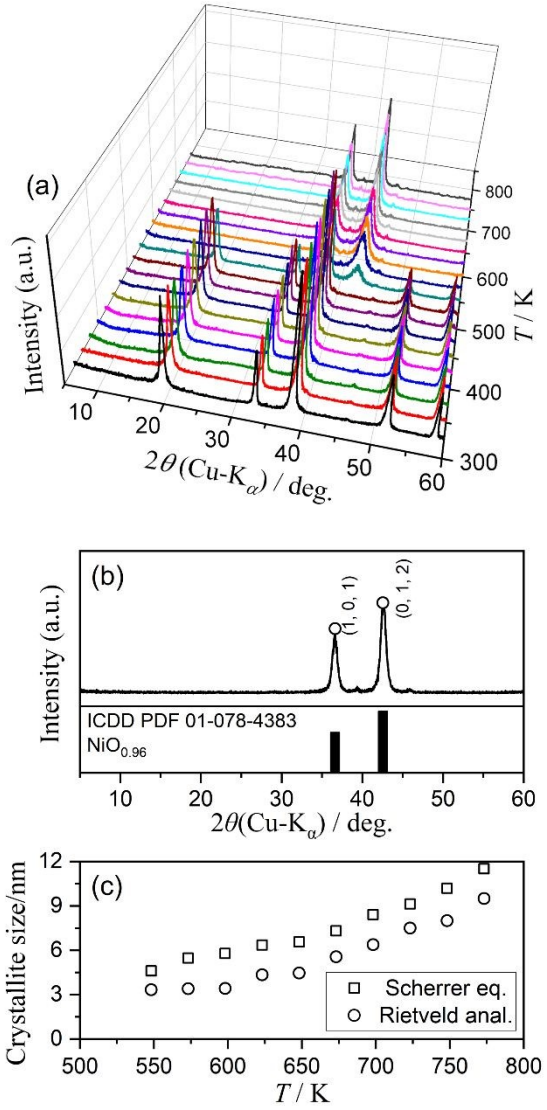


**Figure 2.** XRD patterns of the sample at different temperatures during stepwise isothermal heating in a stream of dry $N_2$ ($q_v$ = 100 cm$^3$ min$^{-1}$): (a) changes in the XRD pattern, (b) XRD pattern at 773 K, and (c) changes in the crystallite size with temperature, calculated using the Scherrer's equation and Rietveld refinement analysis.

### 3.3 Thermal decomposition in a stream of dry $N_2$

Figures S7 and S8 illustrate the variations of the TG–derivative TG (DTG)–DTA curves with the measurement parameters of $m_0$ and $q_v$, respectively. The thermoanalytical (TA) curves exhibited systematical shifts to higher temperatures with increasing $m_0$ (Figure S7). The observed phenomena indicated that the reaction rate is retarded by the effects of self-generated water vapor and self-cooling. As $m_0$ increases, the thickness of the sample bed also increases, thereby hindering diffusional removal of water vapor evolved by the reaction in the bed. In such conditions, the reaction progresses from the upper surface of the sample bed to the bottom.[49-51] Additionally, the self-cooling effect, attributable to the endothermic thermal decomposition, results in a deviation of the sample temperature variation from the linearly increasing temperature that has been programmed for the measurement.[52, 53] This effect is particularly pronounced for the larger $m_0$ value. Conversely, the $q_v$ value demonstrated no significant impact on the TA curves, as demonstrated in Figure S8. This observation indicates that the inert gas flow may not be adequately effective in removing the evolved water vapor from the sample bed in this reaction. While recognizing

the inevitable influence of mass and heat transfer phenomena on the experimental TA curves, the $m_0$ and $q_v$ values for the TG–DTA measurements in a stream of dry $N_2$ were selected to be 5.00 mg and 300 $cm^3$ $min^{-1}$, respectively, by considering the stability and signal/noise ratio of the measured TA curves.

Figure 3 shows the TG–DTG or TG–DTG–temperature profile curves for the thermal decomposition of $Ni(OH)_2$ in a stream of dry $N_2$, recorded with different temperature program modes. Under linear nonisothermal conditions (Figure 3(a)), the TG–DTG curves exhibited the three distinguishable mass loss steps. The initial step with slight mass loss ($\Delta m_1$ = 1.2 ± 0.3%) was followed by a primary mass loss step ($\Delta m_2$ = 16.1 ± 0.4%), and a subsequent step with slow mass loss ($\Delta m_3$ = 3.3 ± 0.3%). The total mass loss of 20.6 ± 0.4% observed during the heating of the sample from 300 to 873 K was slightly larger than the calculated mass loss value of 19.4% according to eq. (1). The sum of the mass loss ratios attributed to the second and third mass loss steps, with reference to the sample mass observed after the first mass loss process was completed ($m_0' = m_0 - \Delta m_1$), was calculated to be 19.6 ± 0.4%, indicating an excellent correspondence to the calculated value for the thermal decomposition of $Ni(OH)_2$. An increase in $\beta$ caused a systematic shift in the TG–DTG curves of the primary mass loss step to higher temperatures. In contrast, the initial mass loss step did not demonstrate the variation with $\beta$ value. The third mass loss step exhibited a shift of the TG–DTG curves to higher temperatures with increasing $\beta$ values. However, the shift width was found to be more restricted in comparison with that observed for the second mass loss step.



View Article Online
DOI: 10.1039/D6CP00975A



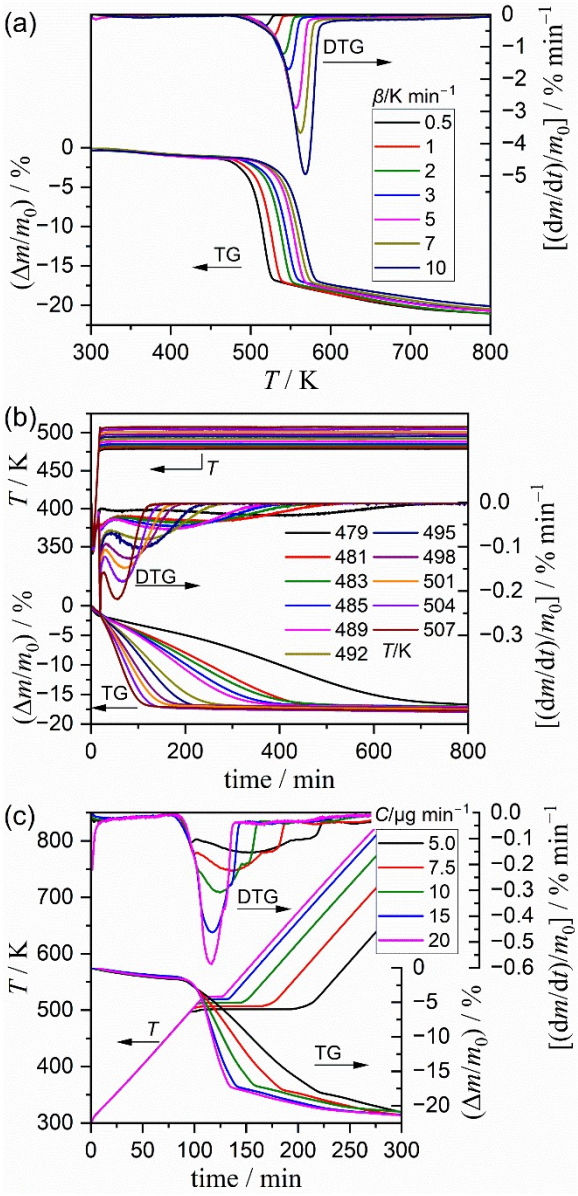


**Figure 3.** TG–DTG or TG–DTG–temperature profile curves for the thermal decomposition of $Ni(OH)_2$ in a stream of dry $N_2$ ($q_v$ = 300 cm$^3$ min$^{-1}$), recorded with different temperature program modes: (a) linear nonisothermal mode at varying $\beta$ values ($m_0$ = 5.00 ± 0.01 mg), (b) isothermal mode at varying $T$ values ($m_0$ = 5.01 ± 0.02 mg), and (c) stepwise isothermal mode at varying $C$ values ($m_0$ = 4.99 ± 0.03 mg).

The TG–DTG curves recorded in the isothermal mode (Figure 3(b)) exhibited two mass loss steps. The initial mass loss step ($\Delta m_1$ = 1.2 ± 0.2%) occurred during the linear heating of the sample from 300 K to the preset temperature for the subsequent isothermal holding. The second mass loss step was observed under isothermal conditions ($\Delta m_2$ = 15.9 ± 0.5%). The mass loss ratios of the first and second mass loss steps were consistent with those observed under linear nonisothermal conditions. The third mass loss step observed in the linear nonisothermal mode did not occur under isothermal conditions examined in this study, due to the limited crystal growth of NiO at these temperatures. It is imperative to note that the presence of the two reaction stages was anticipated during the second mass loss step under isothermal conditions, evidenced by an inflection in the mass loss curve midway through the TG curves and two distinguishable DTG peaks appeared during the second mass loss step. The TG–

DTG curves during the second mass loss process demonstrated a systematic prolongation along the time axis with decreasing $T$ value. The TG–DTG curves recorded in the stepwise isothermal mode (Figure 3(c)) clearly represented three mass loss steps occurring during the initial temperature increasing, isothermal holding, and subsequent temperature increasing sections. The total mass loss ratio of 21.1 ± 0.5% was equivalent to that observed under linear nonisothermal conditions within the standard deviation. The mass loss ratios of the individual mass loss steps were also corresponded to those determined under linear nonisothermal conditions: $\Delta m_1$ = 1.4 ± 0.2%, $\Delta m_2$ = 16.2 ± 0.4%, and $\Delta m_3$ = 3.4 ± 0.1%. The temperature profile during the second mass loss step systematically shifted to higher temperatures with increasing $C$ value. The DTG curves under stepwise isothermal conditions also indicated the presence of two reaction stages in the second mass loss step, which exhibited two distinguishable DTG peaks.

In summary, the thermal decomposition of $Ni(OH)_2$ occurred via three-step mass loss process under linear nonisothermal and stepwise isothermal conditions. The similar mass loss behavior comprising the initial step of the dehydration of absorbed or included water molecules in the $Ni(OH)_2$ agglomerate, followed by the primary step of the thermal decomposition of $Ni(OH)_2$ and subsequent evolution of trapped water accompanied by the crystal growth of NiO has been generally observed for the thermal decomposition of $Ni(OH)_2$ samples with various morphological characteristics, reported previously.[14-21] In order to grasp the multistep thermal decomposition behavior from the kinetic standpoint, the overall thermal decomposition process included three mass loss steps was subjected to the isoconversional kinetic analysis using the Friedman plot.[54] For kinetic analysis, the TG–DTG curves recorded under linear nonisothermal and stepwise isothermal conditions were converted to the kinetic data of a series of data points comprising time ($t$), $T$, $\alpha$, and the normalized reaction rate ($d\alpha/dt$), for which the $\alpha$ value was calculated with reference to the total mass loss of the three-step process.

$$\alpha(t) = \frac{m(t) - m_0}{m_f - m_0}, \tag{2}$$

where $m(t)$ and $m_f$ are the sample mass at time $t$ and that after the mass loss process was completed.

The procedure and results of the isoconversional kinetic analysis as a preliminary kinetic approach are detailed in Section S3-2 of the Supporting Information, with the Friedman plots at various $\alpha$ values represented in Figure S9. In summary, the preliminary kinetic analysis suggested that the thermal decomposition of $Ni(OH)_2$ is composed of four partially overlapping reaction steps, including the desorption of absorbed or included water molecules, the thermal decomposition of $Ni(OH)_2$ via two reaction steps, and the evolution of the trapped water molecules in the NiO product. In addition, it was confirmed that the kinetic data obtained from the TG–DTG curves provided relevant kinetic relationships for the primary mass loss step, thereby, it is interpreted that the primary mass loss step is the actual thermal decomposition process of $Ni(OH)_2$.

Consequently, the extraction of the kinetic data for the primary mass loss step, composed of two reaction steps, from the overall kinetic data was subjected as the subsequent kinetic approach. The DTG curves recorded under linear nonisothermal conditions were deconvoluted into individual peaks corresponding to the component reaction steps using statistical functions ($F(t)$) (mathematical deconvolution analysis (MDA) [25, 55-58]).

$$\frac{dm}{dt} = \sum_{i=1}^{N} F_i(t), \tag{3}$$

where $N$ = 4 for the reaction under investigation. The Weibull function (eq. (S3)) was selected for all component

peaks as a potential $F(t)$ to provide a statistically significant fit to the overall DTG peak after examining using various $F(t)$. Figure 4 shows typical fitting result of the overall DTG curve for the thermal decomposition of $Ni(OH)_2$ at a $\beta$ of 2 K min$^{-1}$ in a stream of dry $N_2$ via MDA using Weibull function. The analogous results for the reaction at different $\beta$ values are illustrated in Figure S10. The contributions ($c_i$) of each reaction step $i$ were evaluated from the area ratio of the deconvoluted DTG peaks (Figure S11). Overall, the $c_i$ values for individual reaction steps remained unchanged at varying $\beta$ values: $c_1 = 0.05 \pm 0.01$, $c_2 = 0.14 \pm 0.04$, $c_3 = 0.64 \pm 0.03$, and $c_4 = 0.16 \pm 0.02$. This observation is regarded as the necessary condition for the assumption of the independent multistep process.

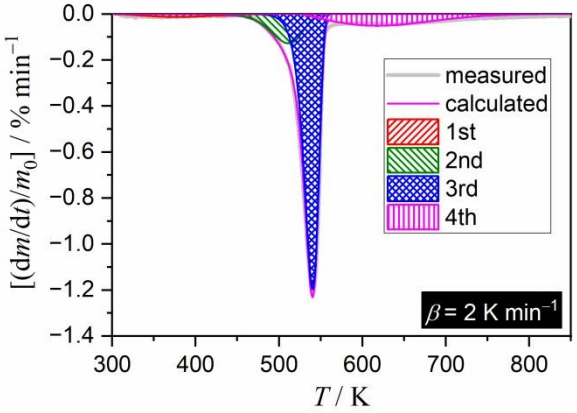


**Figure 4.** Typical fitting result of the overall DTG curves for the thermal decomposition of $Ni(OH)_2$ at a $\beta$ of 2 K min$^{-1}$ in a stream of dry $N_2$ via MDA using Weibull function.

In addition, each series of DTG peaks of individual reaction steps at varying $\beta$ values was obtained as the result of MDA (Figure S12). In each reaction step, the kinetic curves shifted systematically to higher temperatures with increasing $\beta$ value. The kinetic data for individual reaction steps were formally analyzed via the isoconversional method (Friedman plot)[54] and subsequent master plot method.[59-64] The formal kinetic analysis procedures and results are detailed in the Section S3-4 of the Supplementary Information. In summary, the primary reaction process composed of the second and third reaction steps were characterized by individual constant $E_a$ values during each reaction step, while the first and fourth reaction steps exhibited a systematic variation in $E_a$ value as the reaction progressed (Figure S13). The experimental master plots for the second and third reaction steps exhibited the maximum reaction rate midway through each reaction step. In contrast, the rate behavior of the first and fourth reaction steps was characterized by experimental master plots with a concave deceleration curve, indicative of a diffusion-controlled process. This observations for the first and fourth reaction steps are explainable when the reaction steps are regarded as the removal of included or trapped water molecules from the $Ni(OH)_2$ and NiO product. The kinetic parameters for each reaction step determined by the formal kinetic analysis for the kinetic data separated via MDA are enumerated in Table S1.

The kinetic parameters for each reaction step determined by the formal kinetic analysis of the kinetic data obtained via MDA (Table S1) were further optimized based on the cumulative kinetic equation (kinetic deconvolution analysis (KDA) [25, 55, 56, 65]).

View Article Online
DOI: 10.1039/D6CP00975A

$$\frac{\mathrm{d}\alpha}{\mathrm{d}t} = \sum_{i=1}^{N} c_i A_i \exp\left(-\frac{E_{\mathrm{a},i}}{RT}\right) f_i(\alpha_i)$$

$$\text{with} \quad \sum_{i=1}^{N} c_i = 1 \quad \text{and} \quad \sum_{i=1}^{N} c_i \alpha_i = \alpha, \tag{4}$$

where $A_i$ and $E_{\mathrm{a},i}$ are the Arrhenius preexponential factor and apparent activation energy of the reaction step $i$, respectively. $R$ is the gas constant. The kinetic model function, denoted by $f_i(\alpha_i)$, describes the changes in the reaction rate in the reaction step $i$ with increasing $\alpha_i$ values. For the practical KDA, the empirical kinetic model function, known as the Šesták–Berggren model (SB($m_i$, $n_i$, $p_i$)),[66-68] was employed.

$$f_i(\alpha_i) = \alpha_i^{m_i}(1-\alpha_i)^{n_i}\left[-\ln(1-\alpha_i)\right]^{p_i} \tag{5}$$

The SB model with three kinetic exponents was utilized to ensure the precise extraction of the kinetic curves for each component reaction step. This model demonstrates a higher degree of flexibility in comparison with the truncated SB model that incorporates two kinetic exponents. The kinetic parameters listed in Table S1 were set to eq. (4) as the initial values. Subsequently, all kinetic parameters were simultaneously optimized to minimize the square sum of the residues when fitting the overall experimental kinetic curve with calculated curve.

$$F = \sum_{j=1}^{M} \left[\left(\frac{\mathrm{d}\alpha}{\mathrm{d}t}\right)_{\mathrm{exp},j} - \left(\frac{\mathrm{d}\alpha}{\mathrm{d}t}\right)_{\mathrm{cal},j}\right]^2, \tag{6}$$

where $M$ is the total number of numerical data points in each kinetic curve. The subscripts of exp and cal denote experimental and calculated d$\alpha$/d$t$ values, respectively.

The typical results of KDA are illustrated in Figure 5. Initially, all kinetic parameters for individual reaction steps under linear nonisothermal conditions at various $\beta$ values were optimized via KDA, yielding a statistically significant fit to the experimental curves, irrespective of $\beta$ (Figures 5(a) and S14). The optimized kinetic parameters for each experimental kinetic curve were practically invariant among those at different $\beta$ values. The average values of the optimized kinetic parameters are enumerated in Table S2. Subsequently, the experimental kinetic curves under isothermal and stepwise isothermal conditions were also subjected to KDA using the optimized kinetic parameters for the reactions under linear nonisothermal conditions (Table S2) as the initial values. Notably, the experimental kinetic curves under isothermal conditions were analyzed as composed of the partially overlapping three reaction steps, because the fourth reaction step observed under linear nonisothermal and stepwise isothermal conditions has not been traced under isothermal conditions (Figure 3). The experimental kinetic curves under isothermal conditions were successfully fitted via KDA as the three-step process irrespective of the measurement temperature (Figures 5(b) and S15). The optimized kinetic parameters at each constant temperature exhibited minimal variations with the measurement temperature, indicating a limited value of standard deviation for the average values (Table S3). In addition, the optimized kinetic parameters for the first to third reaction steps under isothermal conditions were comparable to those under linear nonisothermal conditions. The analogous KDA results were attained for the four-step thermal decomposition process under stepwise isothermal conditions at various $C$ values (Figures 5(c) and S16; Table S4). The KDA results demonstrate that the kinetic behavior of the individual reaction steps of the overall thermal decomposition of $Ni(OH)_2$ remains constant across a range of heating conditions

and program modes.

View Article Online
DOI: 10.1039/D6CP00975A



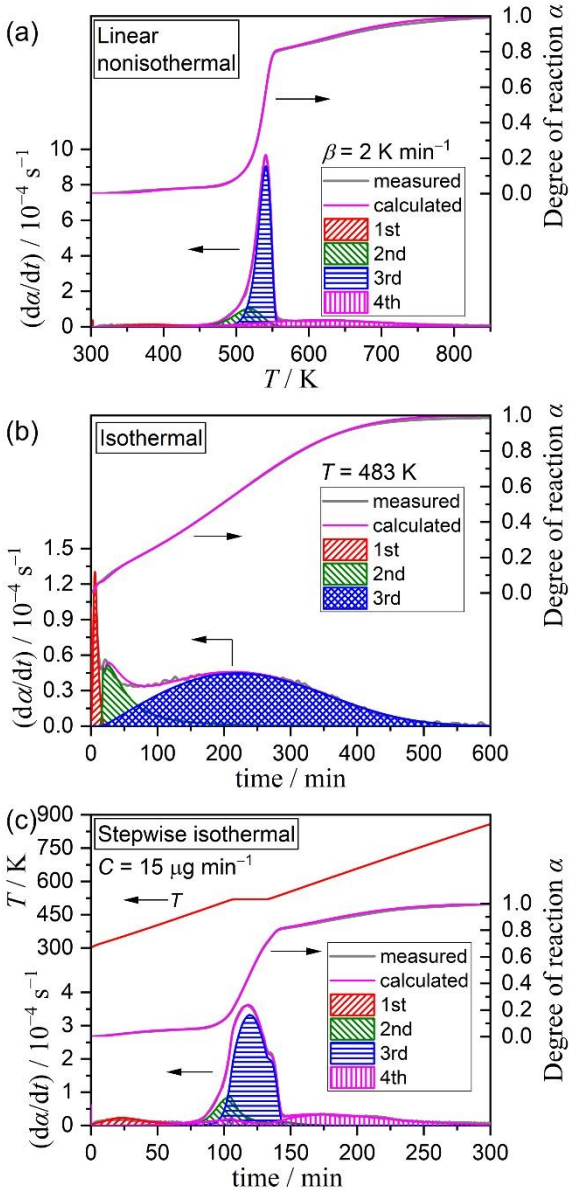


**Figure 5.** Typical results of KDA for the thermal decomposition of $Ni(OH)_2$ under conditions of different heating program modes in a stream of dry $N_2$: (a) linear nonisothermal conditions at $\beta = 2$ K min$^{-1}$, (b) isothermal conditions at $T = 483$ K, and (c) stepwise isothermal conditions at $C = 15$ μg min$^{-1}$.

The refinement of the multistep kinetic description via KDA for the reactions under different heating modes provided us a series of the kinetic curves for the second and third reaction steps that constituting the primary reaction process of the thermal decomposition. The resulting kinetic curves are illustrated in Figures S17 and S18 for the second and third reaction steps, respectively. The ratio of $c_2$:$c_3$ of the extracted kinetic curves were determined to be 0.18 ± 0.02: 0.82 ± 0.02. Each separated reaction step was expected to be able to describe as the single-step kinetic process controlled by a rate-determining step with a specific physico-geometrical constraint. Therefore, the formal kinetic approach based on the isoconversional and master plot methods were reexamined for the second and third reaction steps over different heating modes including linear nonisothermal, isothermal, and stepwise

View Article Online
DOI: 10.1039/D6CP00975A

isothermal modes. The results of the formal kinetic analysis are demonstrated in Figure 6. Based on the fundamental kinetic equation (eq. (S1)), the Friedman plots at various $\alpha_i$ values were examined for each reaction step:

$$\ln\left(\frac{\mathrm{d}\alpha_i}{\mathrm{d}t}\right) = \ln\left[A_i f_i(\alpha_i)\right] - \frac{E_{\mathrm{a},i}}{RT} \quad (7)$$

As demonstrated in Figures 6(a) and (b) for the second and third reaction steps, respectively, the Friedman plots exhibited a statistically significant linear correlation irrespective of $\alpha_i$ values in both reaction steps. It is noteworthy that the linear correlation of the Friedman plot was superior in the third reaction step. This phenomenon can be attributed to the third reaction step, which dominated the major stage of the primary reaction process ($c_3 = 0.82 \pm 0.02$), while the second reaction step reflected the initial stage of the primary reaction process with a minor contribution ($c_2 = 0.18 \pm 0.02$). However, the slope of the Friedman plots remained constant at different $\alpha_i$ values for each reaction step. Consequently, the apparent $E_{\mathrm{a},i}$ values calculated from the slope of the Friedman plot were constant during each reaction step (Figures 6(c) and (d)), yielding the average values of $115.3 \pm 3.7$ and $131.4 \pm 1.9$ kJ mol$^{-1}$ ($0.10 \le \alpha_i \le 0.90$) for the second and third reaction steps, respectively. The constant $E_{\mathrm{a},i}$ values during each reaction step fulfill the prerequisite of the assumption of a single-step kinetic process.

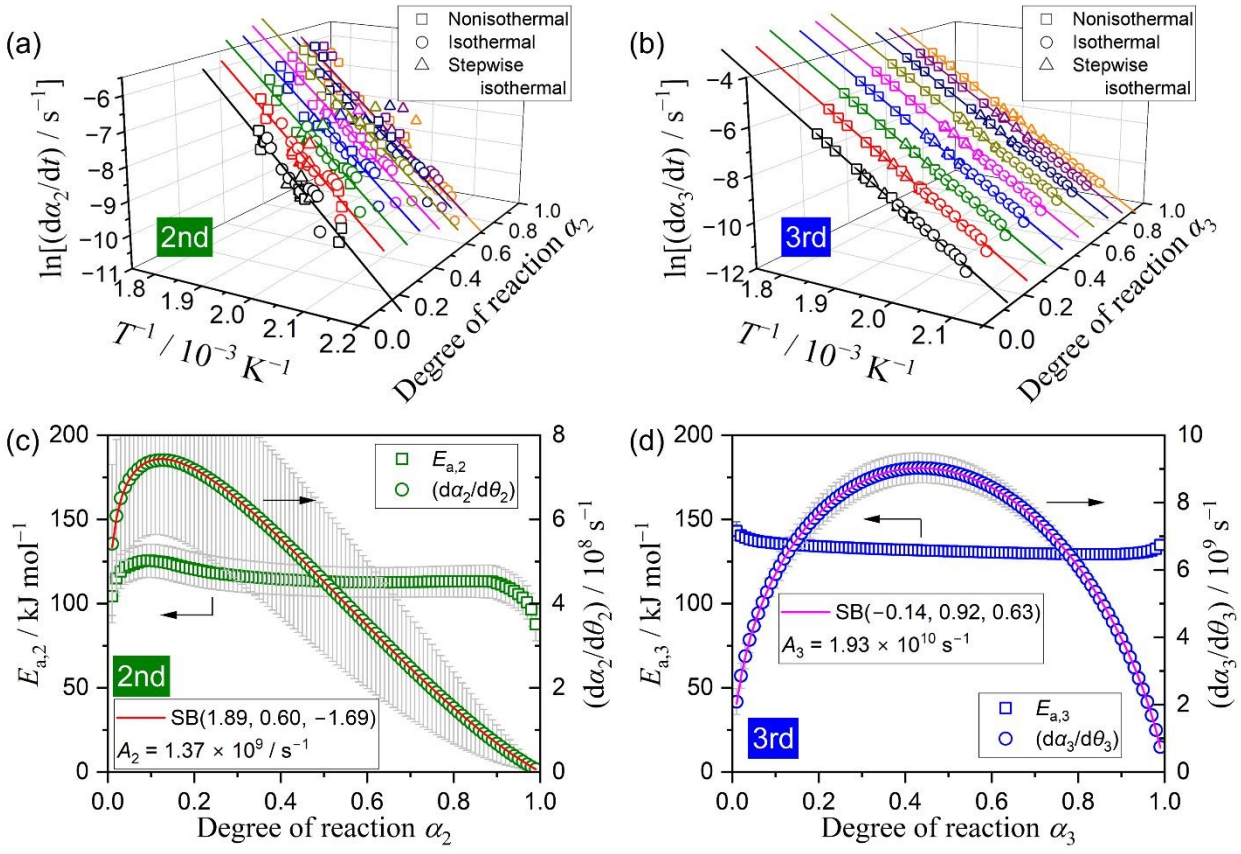


**Figure 6.** Results of the Friedman plot and master plot method analyses for the second and third reaction steps of the thermal decomposition of $Ni(OH)_2$ in a stream of dry $N_2$: (a) Friedman plots at various $\alpha_2$ values (second step), (b) Friedman plots at various $\alpha_3$ values (third step), (c) $E_{\mathrm{a},2}$ value at various $\alpha_2$ values and the experimental master plot of $(\mathrm{d}\alpha_2/\mathrm{d}\theta_2)$ versus $\alpha_2$ (second step), and (d) $E_{\mathrm{a},3}$ value at various $\alpha_3$ values and the experimental master plot of $(\mathrm{d}\alpha_3/\mathrm{d}\theta_3)$ versus $\alpha_3$ (third step).

View Article Online
DOI: 10.1039/D6CP00975A

For each reaction step characterized by the individual $E_{a,i}$ values, the hypothetical reaction rate ($d\alpha_i/d\theta_i$) at infinite temperature can be calculated at various $\alpha_i$ values.[59-64]

$$\frac{d\alpha_i}{d\theta_i} = \left(\frac{d\alpha_i}{dt}\right) \exp\left(\frac{E_{a,i}}{RT}\right) = A_i f_i(\alpha_i)$$

$$\text{with} \qquad \theta_i = \int_0^t \exp\left(-\frac{E_{a,i}}{RT}\right) dt\,, \qquad (8)$$

where $\theta_i$ is Ozawa's generalized time for the reaction step $i$, which is the hypothetical reaction time at infinite temperature.[59, 60] The plot of $d\alpha_i/d\theta_i$ versus $\alpha_i$ can be treated as an experimental master plot describing the variation in the reaction rate as the reaction progresses. The experimental master plots exhibited distinct shapes for the second and third reaction steps (Figures 6(c) and (d), respectively). According to eq. (8), the $A_i$ values of the individual reaction steps were determined by fitting the experimental master plots using SB($m_i$, $n_i$, $p_i$), yielding $A_2$ = (1.37 ± 0.01) × $10^9$ $s^{-1}$ and $A_3$ = (1.93 ± 0.01) × $10^{10}$ $s^{-1}$. Although the physical significance of the optimized kinetic exponents in SB($m_i$, $n_i$, $p_i$) was difficult to evaluate because of their nature as empirical parameters to fit the experimental master plot with high flexibility, the kinetic behavior of the second and third reaction steps can be fully reproduced using the apparent kinetic parameters enumerated in Table 1.



**Table 1.** Kinetic parameters for the second and third reaction steps of the thermal decomposition of $Ni(OH)_2$ across different heating conditions in a stream of dry $N_2$, determined from the separated kinetic data via KDA using the Friedman plot and master plot methods

| Reaction step, $i$ | $c_i/(c_2+c_3)$, [a] | $E_{a,i}$ / kJ mol$^{-1}$, [b] | $\frac{d\alpha_i}{d\theta_i} = A_i f_i(\alpha_i)$ with $f_i(\alpha_i) = \alpha_i^{m_i}(1-\alpha_i)^{n_i}[-\ln(1-\alpha_i)]^{p_i}$ | | | | |
|---|---|---|---|---|---|---|---|
| | | | $A_i$ / s$^{-1}$ | $m_i$ | $n_i$ | $p_i$ | $R^{2}$, [c] |
| 2 | 0.18 ± 0.02 | 115.3 ± 3.7 | (1.37 ± 0.01) × $10^9$ | 1.89 ± 0.03 | 0.60 ± 0.01 | –1.69 ± 0.03 | 0.9999 |
| 3 | 0.82 ± 0.02 | 131.4 ± 1.9 | (1.93 ± 0.01) × $10^{10}$ | –0.14 ± 0.01 | 0.92 ± 0.01 | 0.63 ± 0.01 | 0.9999 |

[a] Averaged over different heating conditions.
[b] Averaged over $0.10 \le \alpha_i \le 0.90$.
[c] Determination coefficient of the nonlinear least-squares analysis.

As illustrated in Figure S19, the experimental master plots of individual reaction steps were reanalyzed using physicochemical or physico-geometrical kinetic model functions. The experimental master plot for the second reaction step exhibited linear deceleration behavior after the brief initial acceleration stage. The observed rate behavior corresponds to the first-order kinetic model (F1): $f(\alpha) = 1 - \alpha$ (Figure S19(a)). Because the second reactions step is characterized as the initial stage of the primary thermal decomposition process with a limited contribution ($c_2/(c_2 + c_3) = 0.18$), the kinetic obedience to F1 can be interpreted as the consumption of the selected reactive sites of the sample, which presumably present on the surface of the $Ni(OH)_2$ agglomerates. Besides, the experimental master plot of the third reaction step, which is the major step of the primary thermal decomposition process ($c_3/(c_2 + c_3) = 0.82$), exhibited the maximum reaction rate midway through the reaction step. Assuming homogeneous-like rate behavior, the rate behavior comprising the initial acceleration and subsequent deceleration is explained by an autocatalytic reaction as expressed by the extended Prout–Tompkins model (ePT($m$, $n$)).[69]

$$\mathrm{ePT}(m,n): f(\alpha) = \alpha^m (1-\alpha)^n \tag{9}$$

The experimental master plot of the third reaction step was satisfactorily fitted with ePT(0.52, 0.70) (Figure S19(b)), which is comparable to SB($m$, $n$, $p$). Considering heterogeneous characteristics of the physico-geometrical constrains of the reaction mechanisms, two distinct models are worth examination to describe the rate behavior with the maximum reaction rate occurring midway through the reaction. One is the nucleation–growth-type model described by the Johnson–Mehl–Avrami–Erofeev–Kolmogorov model (JMA($m$)).[70-75]

$$\mathrm{JMA}(m): f(\alpha) = m(1-\alpha)\left[-\ln(1-\alpha)\right]^{1-1/m}, \tag{10}$$

where the exponent $m$ is so-called Avrami exponent. The experimental master plot was satisfactory fitted with JMA(2.39). The Avrami exponent of $m \approx 2.5$ is explained by a constant rate nucleation and 1.5-dimensional growth of the nuclei controlled by chemical process or a constant rate nucleation and three-dimensional growth of the nuclei controlled by diffusion process. The random nucleation in the matrix of $Ni(OH)_2$ and the expansion of the volume of product phase is expected based on JMA($m$) model. The other possible kinetic model is the contracting-geometry reaction with the acceleration of the linear advancement rate of the reaction interface described by the Galway and Hood model (GH($n$)).[76, 77]

$$\mathrm{GH}(n): f(\alpha) = 2n(1-\alpha)^{1-1/n}\left[1-(1-\alpha)^{1/n}\right]^{1/2}, \tag{11}$$

where exponent $n$ corresponds to the contraction dimension of the reaction interface. However, any satisfactory fits of the experimental master plot were not achieved with GH($n$) (Figure S19(b)). An alternative kinetic description was also examined assuming a physico-geometrical consecutive process comprising a surface reaction and subsequent interfacial shrinkage as described by a Mampel model.[78-81] However, the combined kinetic model was unable to adequately represent the overall kinetic behavior of the third reaction step under isothermal conditions.

### 3.4 Thermal decomposition in a stream of wet $N_2$ with various atmospheric water vapor pressures

As illustrated in Figure 7, the primary mass loss process of the thermal decomposition of $Ni(OH)_2$ is influenced by $p(H_2O)_{ATM}$. The TG–DTG curves under linearly increasing temperature conditions exhibited a systematic shift to higher temperatures with increasing $p(H_2O)_{ATM}$ value, indicating the retardation effect due to $p(H_2O)$. It is important to note that this phenomenon is characteristic of the reversible thermal decomposition process. In the context of thermal decomposition processes of this nature, a more pronounced shift in the

thermoanalytical curves towards higher temperatures with an increase in $p(H_2O)_{ATM}$ is generally observed, particularly within a reduced $p(H_2O)$ range. The retardation effect of $p(H_2O)$ on the kinetics of the thermal decomposition of solids should be considered with reference to the equilibrium pressure of the gaseous product ($P_{eq}(T)$). The changes in the $P_{eq}(T)$ value with temperature are demonstrated in Figure S20, which was calculated using the literature values of the thermodynamic parameters of the reaction system.[82] The extended kinetic equation that describes the reaction as a function of $T$, $\alpha$, and $p(H_2O)$ has been obtained by introducing an accommodation function (AF; $h(p(H_2O), P_{eq}(T))$) into the fundamental kinetic equation. [29, 40, 41]

$$\frac{d\alpha}{dt} = A \exp\left(-\frac{E_a}{RT}\right) f(\alpha) h\left(p(H_2O), P_{eq}(T)\right) \quad (12)$$

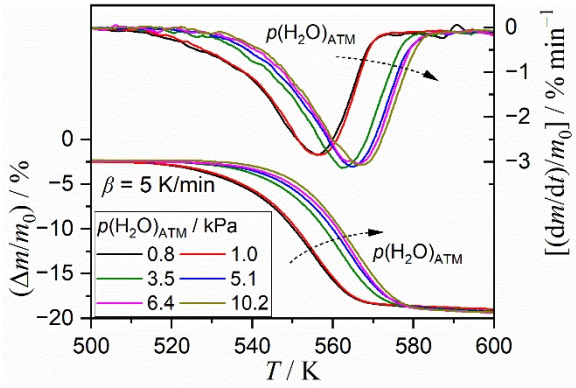


**Figure 7.** TG–DTG curves for the primary mass loss process of the thermal decomposition of $Ni(OH)_2$ under linear nonisothermal conditions at a $\beta$ of 5 K min$^{-1}$ in a stream of wet $N_2$ with different $p(H_2O)_{ATM}$ values.

Figure 8 shows the TG–DTG curves recorded under linear nonisothermal conditions at different $\beta$ values and isothermal conditions at different $T$ values in a stream of wet $N_2$ with a $p(H_2O)_{ATM}$ value of 3.6 kPa. The analogous at $p(H_2O)_{ATM}$ values of 0.8 and 9.2 kPa are represented in Figures S21 and S22, respectively. Irrespective of $p(H_2O)_{ATM}$ value, the TG–DTG curves exhibited three mass loss process and systematically shifted to higher temperatures with increasing $\beta$ value ((a) in Figures 8, S21, and S22). In the measurement using isothermal mode, the initial mass loss step was observed during linear heating to the preset isothermal temperature. Thereafter, the primary mass loss process occurred at constant temperature ((b) in Figures 8, S21, and S22). The mass loss rate of the primary mass loss process increased systematically with increasing $T$. The mass loss behavior and its variation with the measurement temperature conditions were comparable to those previously observed for the reaction in a stream of dry $N_2$ (Figure 3).

View Article Online
DOI: 10.1039/D6CP00975A



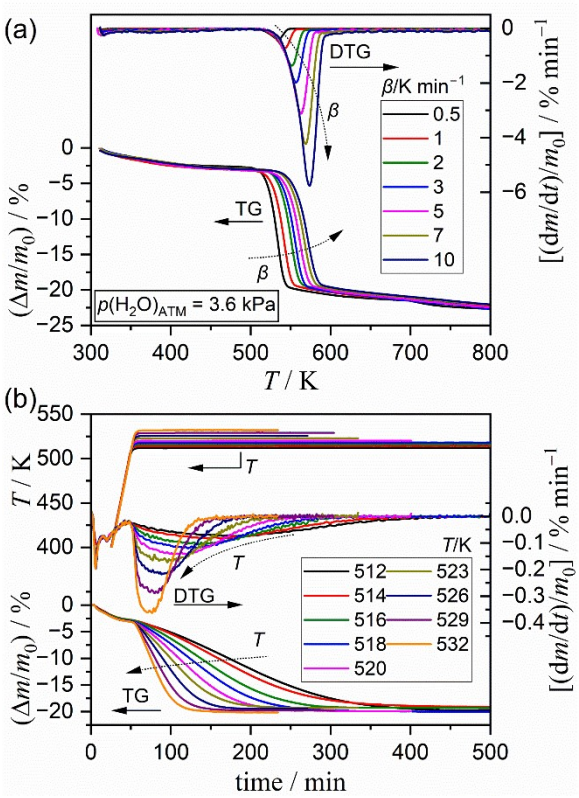


**Figure 8.** TG–DTG curves for the thermal decomposition of $Ni(OH)_2$ under different heating conditions in a stream of wet $N_2$ characterized by $p(H_2O)_{ATM}$ = 3.6 ± 0.1 kPa: (a) linear nonisothermal conditions at various $\beta$ values ($m_0$ = 5.02 ± 0.02 mg) and (b) isothermal conditions at various $T$ values ($m_0$ = 5.01 ± 0.02 mg).

It is important to note that the primary mass loss process occurred at a significantly higher temperatures and at a lower $p(H_2O)$ values with reference to the $P_{eq}(T)$ curve (Figure S20), calculated according to eq. (13).

$$P_{eq}(T) = \exp\left(-\frac{\Delta_r G^\circ}{RT}\right) = \exp\left(-\frac{\Delta_r H^\circ - T\Delta_r S^\circ}{RT}\right), \quad (13)$$

where $\Delta_r G^\circ$, $\Delta_r H^\circ$, and $\Delta_r S^\circ$ are the standard Gibbs energy, enthalpy, and entropy of the reaction. Therefore, as an approximated kinetic approach, the kinetic curves derived from the TG–DTG curves recorded at individual $p(H_2O)_{ATM}$ values were initially analyzed using the fundamental kinetic equation by assuming the AF to be unity, i.e., $h(p(H_2O), P_{eq}(T)) = 1$. The isoconversional kinetic approach to the overall thermal decomposition process using the Friedman plot indicated the establishment of the isoconversional kinetic relationship in the restricted $\alpha$ range corresponding to the primary reaction process, irrespective of the $p(H_2O)_{ATM}$ values (Figures S23, S24, and S25). The kinetic data for the primary reaction process comprising two reaction steps (second and third reaction steps) were extracted from the TG–DTG curves under linear nonisothermal conditions ((a) in Figures 8, S21, and S22) using MDA (Figure S26), as was done for the reaction in a stream of dry $N_2$. The extracted kinetic data for the second and third reaction steps were subjected to the formal kinetic analysis of the conventional Friedman plot (eq. (7)) and master plot method (eq. (8)), yielding the kinetic parameters for each reaction step at individual $p(H_2O)_{ATM}$ values (Table S5). Furthermore, the kinetic parameters determined by the formal kinetic analysis were refined via KDA (Figure S27; Table S6). Using the refined kinetic parameters for the second and third reaction steps under linear nonisothermal conditions as the initial values, the corresponding kinetic data under isothermal conditions

View Article Online
DOI: 10.1039/D5CP00975A

were also extracted from the TG–DTG curves ((b) in Figures 8, S21, and S22) via KDA (Figure S28; Table S7). Through the MDA and KDA procedures, the kinetic data for the second and third reaction steps, which constitute the primary thermal decomposition process of $Ni(OH)_2$, under linear nonisothermal and isothermal conditions in a stream of wet $N_2$ at individual $p(H_2O)_{ATM}$ values were obtained as shown in Figures S29–S34.

The extracted kinetic data of the second and third reaction steps under linear nonisothermal and isothermal conditions at each $p(H_2O)_{ATM}$ value were simultaneously subjected to formal kinetic analysis, in which the effect of $p(H_2O)$ was ignored. The results are detailed in S4-3 section of the Supporting Information, with Figures S35, S36, and Table S8 for the second reaction step and Figures S37, S38, and Table S9 for the third reaction step. Irrespective of the reaction steps, the formal kinetic analysis yielded apparent kinetic parameters that were distinct for the reactions at different $p(H_2O)_{ATM}$ values. Consequently, the consideration of AF in eq. (12) is necessary for a universal kinetic description across different $p(H_2O)_{ATM}$ values. Recently, an analytical form of AF was derived based on the classical theory of surface and interfacial processes, which comprise consecutive/concurrent elementary steps, while assuming one rate-determining step and steady-state conditions for the other steps. [29, 40, 41]

$$h\Big(p(\mathrm{H_2O}),P_{\mathrm{eq}}(T)\Big) = \left(\frac{1}{p(\mathrm{H_2O})}\right)^{a}\left[1-\left(\frac{p(\mathrm{H_2O})}{P_{\mathrm{eq}}(T)}\right)^{b}\right], \tag{14}$$

where the unit of pressure terms is atm. The exponents ($a$, $b$) are relevant to the rate-determining step among the consecutive/concurrent elementary steps in the surface and interfacial processes. Theoretically, the ($a$, $b$) values can have (0, 1) and (1, 1), as well as $a = b$ specifically for the process controlled by the formation of the product crystalline phase.[29, 40, 41] The isoconversional kinetic relationship that is universally applicable to the reactions across varying $p(H_2O)$ values can be expressed by the extended Friedman plot. [29, 40, 41]

$$\ln\frac{\left(\frac{\mathrm{d}\alpha}{\mathrm{d}t}\right)}{h\Big(p(\mathrm{H_2O}),P_{\mathrm{eq}}(T)\Big)} = \ln\big[Af(\alpha)\big] - \frac{E_{\mathrm{a}}}{RT} \tag{15}$$

According to eq. (15), the plot of $\ln[(\mathrm{d}\alpha/\mathrm{d}t)/h(p(\mathrm{H_2O}), P_{eq}(T))]$ versus $T^{-1}$ at a selected $\alpha$ should yield a linear correlation across all data points under different heating conditions at varying $p(H_2O)$ values, when the appropriate ($a$, $b$) values in AF (eq. (14)) are applied.

Initially, the extended Friedman plot was applied to each reaction step by assuming ($a$, $b$) = (0, 1) and (1, 1), while the $p(H_2O)_{ATM}$ value was set for $p(H_2O)$. In both second and third reaction steps, the results did not achieved to reveal a universal isoconversional relationship, yielding individual linear correlations at different $p(H_2O)_{ATM}$ values (Figures S39 and S40, respectively). Therefore, the most appropriate $a = b$ value was optimized through the extended Friedman plot. The results of extended kinetic analysis with the optimized $a = b$ are illustrated in Figure 9. In both reaction steps, universal isoconversional relationship was established with the optimized $a = b$ values of 0.53 and 0.29 for the second and third reaction steps, respectively (Figures 9(a) and (b)). These universal isoconversional relationships were established at various $\alpha_i$ values (Figure S41). Theoretically, the AF with $a = b$ values has been derived for the surface and interfacial processes controlled by the formation of product crystalline phase.[29, 40, 41] However, the slope of the extended Friedman plot varied as the reaction progressed in each step. In the second reaction step, the $E_{a,2}$ value initially increased and subsequently converged to a constant value in the major reaction stage (Figure 9(c)). In contrast, a gradual decline of the $E_{a,3}$ value was observed as the reaction progressed in the third reaction step; however, the observed variation was limited within 10 kJ mol$^{-1}$ (Figure 9(d)).

View Article Online
DOI: 10.1039/D6CP00975A

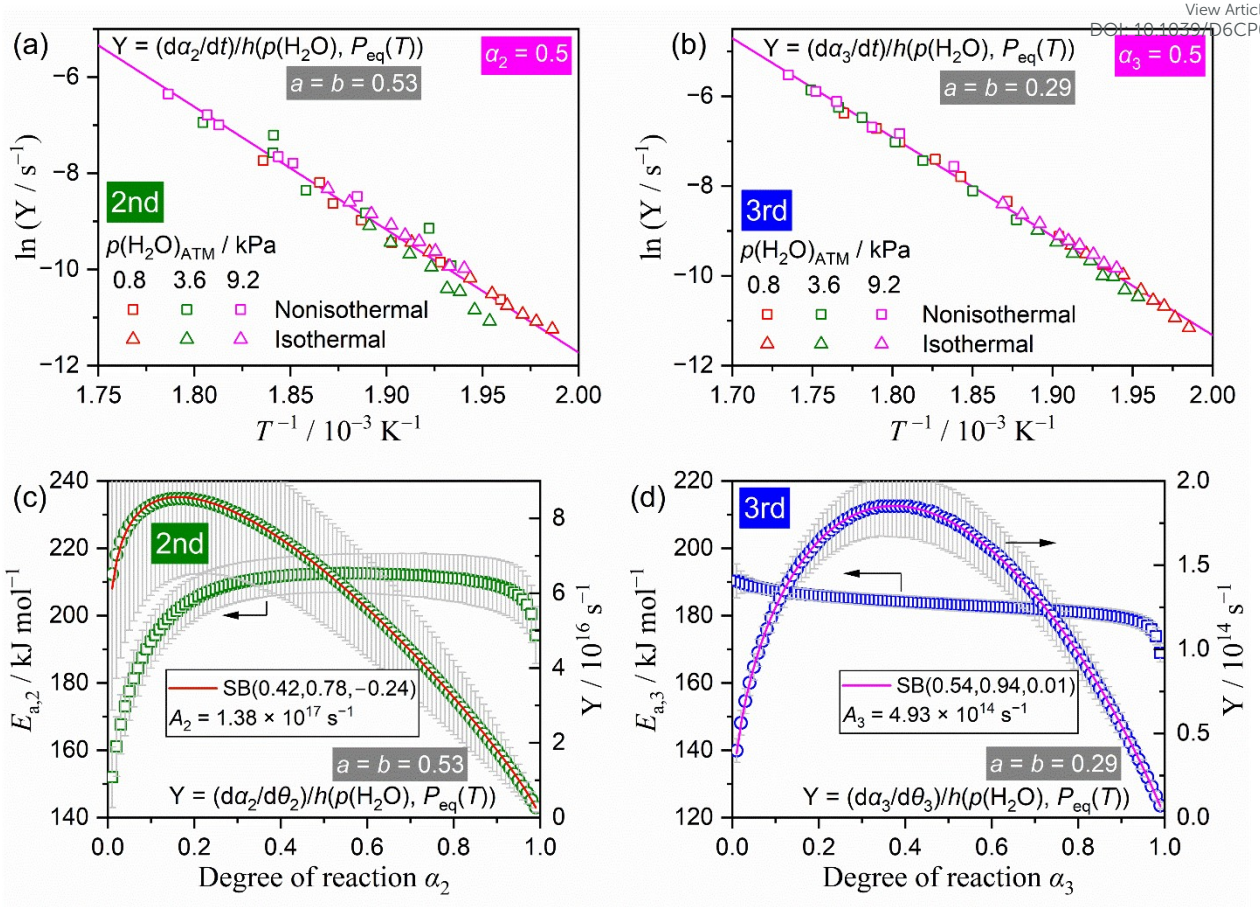


**Figure 9.** Extended kinetic analysis considering the effect of $p(H_2O)_{ATM}$ for the second and third reaction steps of the thermal decomposition of $Ni(OH)_2$ with the optimized $a = b$ value: (a) extended Friedman plot with $a = b = 0.53$ for the second reaction step at $\alpha_2 = 0.5$, (b) extended Friedman plot with $a = b = 0.29$ for the third reaction step at $\alpha_3 = 0.5$, (c) $E_{a,2}$ at various $\alpha_2$ values and the extended experimental master plot with the fitting curve using SB(0.42, 0.78, −0.24) (second reaction step), and (d) $E_{a,3}$ at various $\alpha_3$ values and the extended experimental master plot with the fitting curve using SB(0.54, 0.94, 0.01) (third reaction step).

Assuming that the average $E_{a,i}$ value over the major reaction stage ($0.10 \le \alpha_i \le 0.90$) is representative for the reaction across different $p(H_2O)$ values, the extended experimental master plot can be constructed by calculating $(d\alpha_i/d\theta_i)/h(p(H_2O), P_{eq}(T))$ values at various $\alpha_i$ values. [32, 33, 37, 38, 40, 41]

$$\frac{\left(\frac{d\alpha_i}{d\theta_i}\right)}{h\left(p(H_2O),P_{eq}(T)\right)} = \frac{\left(\frac{d\alpha_i}{dt}\right)\exp\left(\frac{E_{a,i}}{RT}\right)}{h\left(p(H_2O),P_{eq}(T)\right)} = A_i f_i(\alpha_i) \quad (16)$$

The extended experimental master plot for the second reaction step exhibited the maximum reaction rate at the initial stage of the reaction step and subsequently decelerated as the reaction progressed (Figure 9(c)). The shape of the experimental master plot is resembled to that of the second reaction step in a stream of dry $N_2$ (Figure 6(c)); however, the deceleration stage is characterized by a convex shape. The extended experimental master plot for the third reaction step exhibited the maximum reaction midway through the reaction at $\alpha_3 = 0.37$ (Figure 9(d)). The rate behavior comprising the initial acceleration and subsequent deceleration is equivariant to that in a stream of dry $N_2$

View Article Online
DOI: 10.1039/D6CP00975A

(Figure 6(d)). The extended experimental master plots were almost perfectly fitted using the SB($m$, $n$, $p$) function, yielding constant $A_i$ values for individual reaction steps.

Table 2 enumerates the apparent kinetic parameters for the second and third reaction steps determined in the context of universal kinetic description across different $p(H_2O)_{ATM}$ values with the optimized $a = b$ values. As was observed by the comparison of the shapes of the conventional and extended experimental master plots, the rate behavior under isothermal conditions, characterized by the kinetic exponents in SB($m$, $n$, $p$), exhibited a resemble trend between the reactions in a stream of dry and wet $N_2$ in each reaction step. On the other hand, the apparent Arrhenius parameters determined by considering the effect of $p(H_2O)_{ATM}$ were significantly larger than those determined by the conventional kinetic analysis for the reactions in a stream of dry $N_2$ (Table 1). One characteristics of the extended Friedman plot should be addressed to correlate the apparent Arrhenius parameters ($E_a$, $A$) to the intrinsic Arrhenius parameters ($E_{a,int}$, $A_{int}$). The extended Friedman plot simultaneously examines the temperature dependences of reaction rate and $P_{eq}(T)$, which are explained by the Arrhenius and van't Hoff equations, respectively. Comparing the kinetic equations of the conventional and extended Friedman plots (eqs. (7) and (15)), the following relationships between the apparent Arrhenius parameters determined based on the extended kinetic equation (eq. (12)) and the intrinsic Arrhenius parameters have been derived. [31, 32, 40, 41]

$$E_{a,int} \approx E_a - b\Delta_r H^\circ \tag{17}$$

$$A_{int} \approx A\exp\left(-\frac{b\Delta_r S^\circ}{R}\right) \tag{18}$$

The intrinsic Arrhenius parameters, calculated according to eqs. (17) and (18) using literature values of $\Delta_r H^\circ_{298}$ = 48.182 kJ mol$^{-1}$ and $\Delta_r S^\circ_{298}$ = 138.815 J mol$^{-1}$ K$^{-1}$ for the thermal decomposition of $Ni(OH)_2$,[82] exhibited a reduction of the values from the apparent values in both reaction steps, as listed in Table 2. However, the intrinsic Arrhenius parameters were still larger than those determined for the reactions in a stream of dry $N_2$ (Table 1).

**Table 2.** Apparent kinetic parameters for the second and third reaction steps of the thermal decomposition of $Ni(OH)_2$ in a stream of wet $N_2$, determined by considering the effect of $p(H_2O)_{ATM}$ value with optimized $a = b$ value, as well as the intrinsic Arrhenius parameters calculated according to eqs. (17) and (18)

| Reaction step, $i$ | $a = b$ | $E_{a,i}$ / kJ mol$^{-1}$, [a] | $\frac{(d\alpha_i/d\theta_i)}{h\left(p(H_2O),P_{eq}(T)\right)} = A_i f_i(\alpha_i)$ with $f_i(\alpha_i) = \alpha_i^{m_i}(1-\alpha_i)^{n_i}[-\ln(1-\alpha_i)]^{p_i}$ | | | | | Intrinsic Arrhenius parameters, [a] | |
|---|---|---|---|---|---|---|---|---|---|
| | | | $A_i$ / s$^{-1}$ | $m_i$ | $n_i$ | $p_i$ | $R^2$, [b] | $E_{a,i,int}$ / kJ mol$^{-1}$ | $A_{i,int}$ / s$^{-1}$ |
| 2 | 0.53 | 209.5 ± 4.6 | (1.38 ± 0.01) × $10^{17}$ | 0.42 ± 0.03 | 0.78 ± 0.01 | –0.24 ± 0.03 | 0.9999 | 184.2 ± 4.6 | (2.12 ± 0.02) × $10^{13}$ |
| 3 | 0.29 | 183.4 ± 2.0 | (4.93 ± 0.01) × $10^{14}$ | 0.54 ± 0.03 | 0.93 ± 0.01 | 0.01 ± 0.03 | 0.9999 | 169.3 ± 2.0 | (3.64 ± 0.03) × $10^{12}$ |

[a] Averaged over $0.10 \le \alpha_i \le 0.90$.
[b] Determination coefficient of the nonlinear least-squares analysis.



3.5 Universal kinetic description considering atmospheric and self-generated water vapor pressures

Another issue that must be addressed to achieve a rigorous kinetic description is the effect of $p(H_2O)_{SG}$ on the kinetic behavior, as expected from the systematic shift in the TG–DTG curves with varying $m_0$ values. This issue is relevant to both the kinetic results for the reactions in a stream of dry and wet $N_2$ gases, as described in the previous sections. However, the $p(H_2O)_{SG}$ value during the thermal decomposition process is unmeasurable. Recently, an empirical procedure was examined to consider both $p(H_2O)_{SG}$ and $p(H_2O)_{ATM}$ in the universal kinetic description across different $T$ and $p(H_2O)$ values. The effective $p(H_2O)_{EF}$ is empirically defined as the sum of the contributions of $p(H_2O)_{SG}$ and $p(H_2O)_{ATM}$, where the $p(H_2O)_{SG}$ value is assumed to be proportional to the reaction rate. [33, 37, 40, 41]

$$p(H_2O)_{EF} = p(H_2O)_{SG} + d \cdot p(H_2O)_{ATM} = c \cdot \left(\frac{d\alpha}{dt}\right) + d \cdot p(H_2O)_{ATM}, \quad (19)$$

where ($c$, $d$) are the coefficients to determine the contributions of $p(H_2O)_{SG}$ and $p(H_2O)_{ATM}$, respectively. The extended kinetic analysis for the universal kinetic description across varying $T$ and $p(H_2O)_{ATM}$ values, as demonstrated in Figure 9 and Table 2, as well as Figure S41, was reexamined by implementing $p(H_2O)_{EF}$ in $p(H_2O)$ in the extended kinetic equation. The coefficients ($c$, $d$) in eq. (19) were optimized to achieve the best linear correlation for the extended Friedman plot, while maintaining the previously determined $a = b$ values.

Figures S42 and S43 demonstrate the extended kinetic analysis considering both $p(H_2O)_{SG}$ and $p(H_2O)_{ATM}$, as applied to the second and third reaction steps across various $p(H_2O)_{ATM}$ values. In both reaction steps, an enhancement of the linearity of the extended Friedman plots was accomplished through the optimization of the coefficients ($c$, $d$) (Figures S42(a) and S43(a)). The linearity of the extended Friedman plots was guaranteed at various $\alpha_i$ values (Figures S42(b) and S43(b)). The $d$ values for $p(H_2O)_{ATM}$ optimized to achieve the best linearity of the plot were approximately unity during each reaction step, while the optimized $c$ values for $p(H_2O)_{SG}$ varied as the reaction progressed in both reaction steps (Figures S42(c) and S43(c)). However, the variation trends of the $c$ value were distinct between the second and third reaction steps.

In the second reaction step, the optimized $c$ value was negligible in the initial stage and subsequently increased exponentially in the latter stage (Figure S42(c)). The variation trend of the $c$ value indicates that the effect of $p(H_2O)_{SG}$ is negligible in the initial stage of the second reaction step, but increases in the latter stage. The anticipated change in the effect of $p(H_2O)_{SG}$ as the reaction progressed is explainable considering the physico-geometrical constraint of the surface reaction process, for which the initial reaction site is on the surface of the reactant particles, where the evolved water vapor is immediately removed because the site is exposed to atmosphere. However, the reactant surface is gradually covered by the solid product layer as the reaction progresses. Under such physico-geometrical conditions, diffusion of the gaseous product through the surface product layer becomes the necessary process, which induces the increase in the $p(H_2O)_{SG}$ at the reaction site covered by the product layer. Besides, the $c$ value for the third reaction step exhibited an approximately constant value during the primary stage of the third reaction step (Figure S43(c)). Because the third reaction step was characterized by the initial acceleration and subsequent deceleration with the maximum reaction rate midway through in both the reactions in a stream of dry and wet $N_2$, a noticeable increase in $p(H_2O)_{SG}$ is anticipated during the primary stage. The constant $c$ value during the primary stage is indicative of significant effect of $p(H_2O)_{SG}$.

In both reaction steps, the apparent $E_{a,i}$ values exhibited minimal variation from those determined in the

previous analysis step (Table S10), with the effect of $p(H_2O)_{SG}$ being ignored. As the $a = b$ values in each reaction step were maintained unchanged from the previous analysis step, the $E_{a,i,int}$ values calculated according to eq. (17) were also exhibited a minimal change from the previous evaluation. However, the extension of the kinetic analysis by incorporating the effect of $p(H_2O)_{SG}$ enabled the empirical evaluation of the effect of $p(H_2O)_{SG}$ and its variation as the reaction progressed in each reaction step.

It is imperative to acknowledge that the effect of $p(H_2O)_{SG}$ is an inevitable factor for the rigorous kinetic description, even for the reaction occurring in a stream of inert gas with negligible $p(H_2O)_{ATM}$. The conventional kinetic analysis for the reaction in a stream of dry $N_2$, as demonstrated in the previous section, can be upgraded in the context of the extended kinetic analysis, considering both $p(H_2O)_{SG}$ and $p(H_2O)_{ATM}$. All kinetic data for the reactions in a stream of dry $N_2$ were incorporated into the extended kinetic analysis of each reaction step. Figures 10 and 11 illustrate the results of extended kinetic analysis, incorporating the kinetic data in a stream of dry $N_2$, for the second and third reaction steps, respectively. In both reaction steps, the extended Friedman plot exhibited a statistically significant linear correlation including the data points for the reactions in a stream of dry $N_2$ (Figures 10(a) and 11(a)), which was achieved by optimizing the exponents $a = b$ in AF (eq. (14)) and the coefficients ($c$, $d$) in $p(H_2O)_{EF}$ (eq. (19)). The comparable results of linear plot were observed at various $\alpha_i$ values (Figures 10(b) and 11(b)).

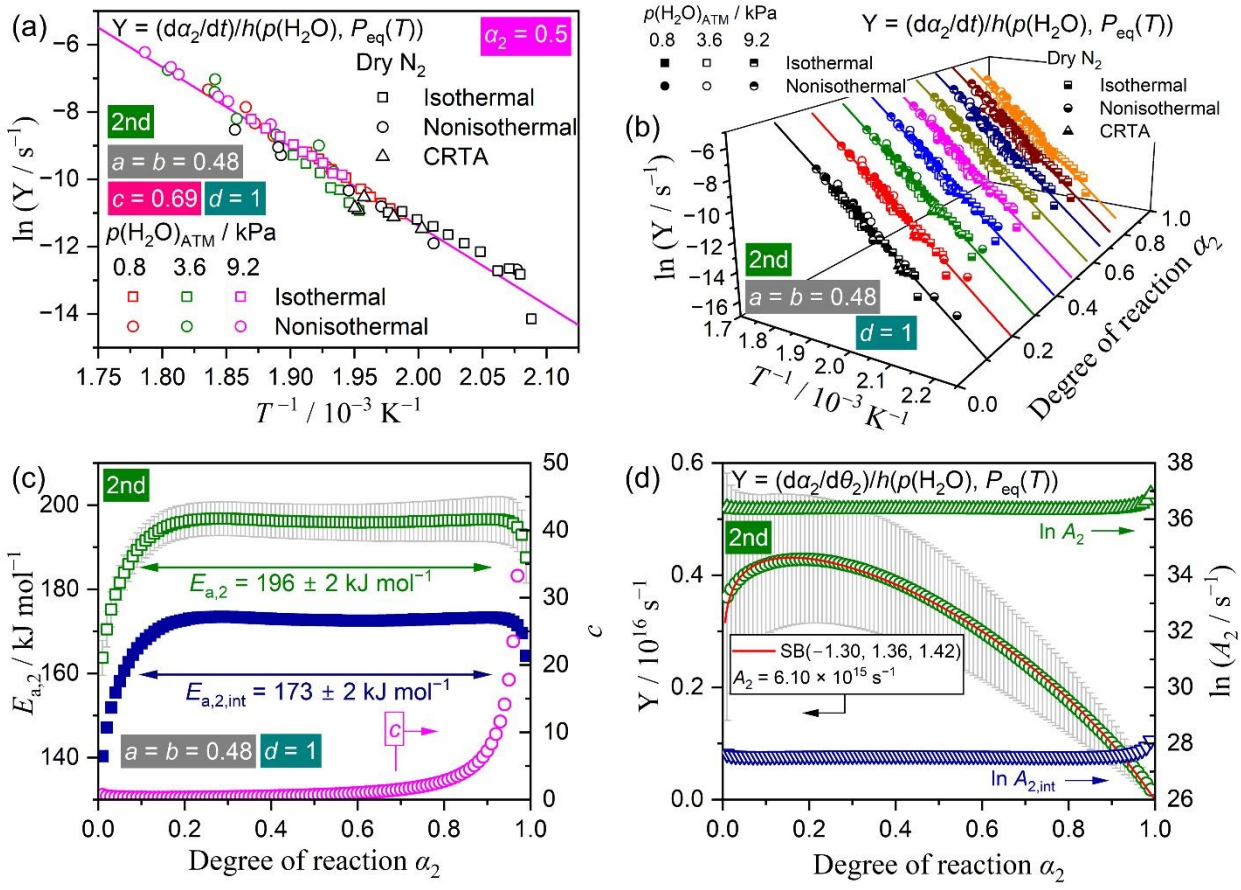


**Figure 10.** Extended kinetic analysis considering the effect of $p(H_2O)_{SG}$ and $p(H_2O)_{ATM}$ for the second reaction step of the thermal decomposition of $Ni(OH)_2$ in a stream of dry and wet $N_2$ with the optimized $a = b$ and coefficient ($c$, $d$) values: (a) extended Friedman plot with $a = b = 0.48$ and ($c$, $d$) = (0.69, 1) at $\alpha_2 = 0.5$, (b) extended Friedman

plots at various $\alpha_2$ values with $a = b = 0.48$ and $d = 1$, while with $c$ value optimized at each $\alpha_2$, (c) optimized $c$ value and apparent and intrinsic $E_{a,2}$ values at various $\alpha_2$ values, and (d) extended experimental master plot with the fitting curve using SB(−1.30, 1.36, 1.42) and the apparent and intrinsic $A_2$ values at various $\alpha_2$ values.



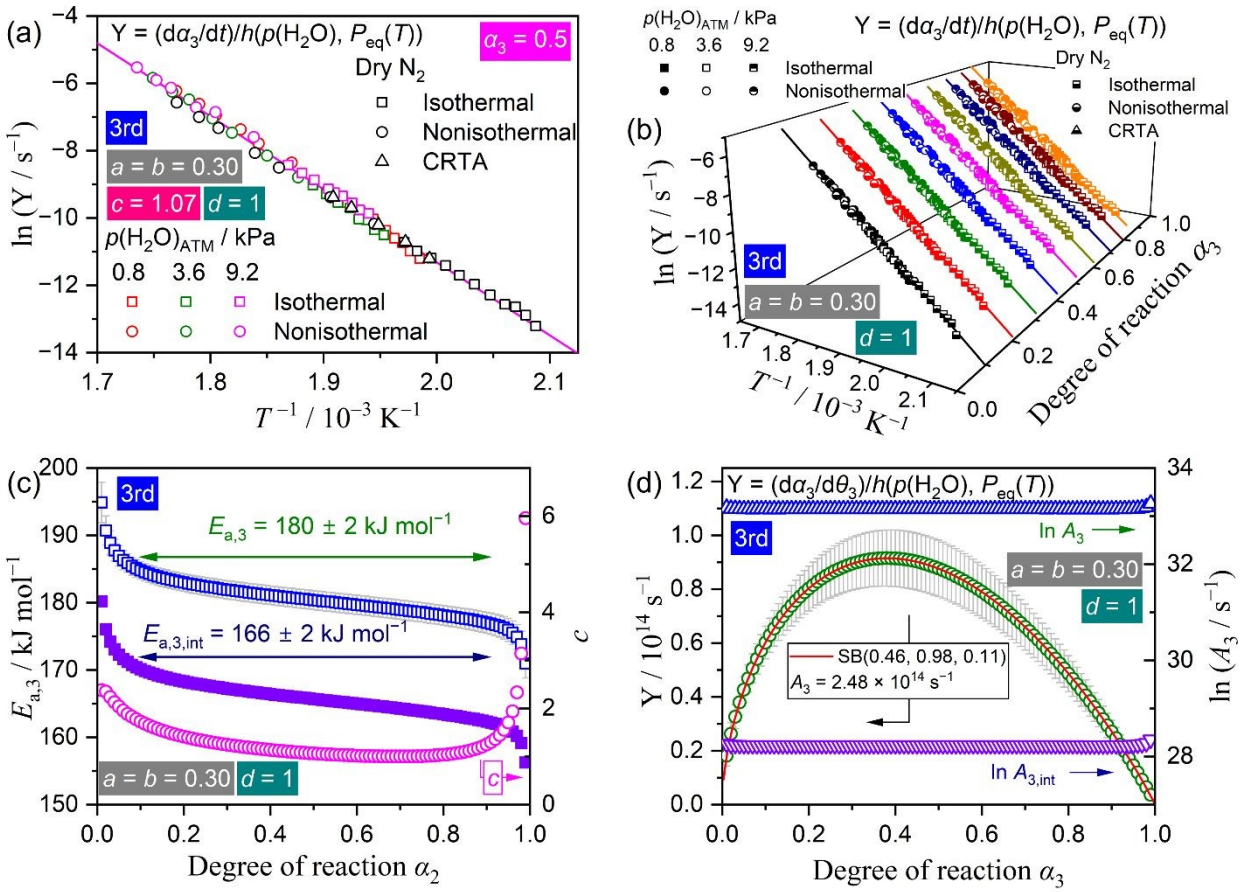


**Figure 11.** Extended kinetic analysis that incorporated the effect of $p(H_2O)_{SG}$ and $p(H_2O)_{ATM}$ for the third reaction step of the thermal decomposition of $Ni(OH)_2$ in a stream of dry and wet $N_2$ with the optimized $a = b$ and coefficient ($c$, $d$) values: (a) extended Friedman plot with $a = b = 0.30$ and ($c$, $d$) = (1.07, 1) at $\alpha_3 = 0.5$, (b) extended Friedman plots at various $\alpha_3$ values with $a = b = 0.30$ and $d = 1$, while with $c$ value optimized at each $\alpha_3$, (c) optimized $c$ value and apparent and intrinsic $E_{a,3}$ values at various $\alpha_3$ values, and (d) extended experimental master plot with the fitting curve using SB(0.46, 0.98, 0.11) and the apparent and intrinsic $A_3$ values at various $\alpha_3$ values.

Extended isoconversional relationships were established with the optimized $a = b$ values of 0.48 and 0.30 for the second and third reaction steps, respectively. The coefficient $d$ for $p(H_2O)_{ATM}$ was estimated to be approximately unity during each reaction step. The trend of the variation in the coefficient $c$ for $p(H_2O)_{SG}$ in the second reaction step (Figure 10(c)), exhibiting negligible value in the initial stage and exponential increase in the latter stage, was equivalent to that evaluated without incorporating the kinetic data in a stream of dry $N_2$ (Figure S42(c)). Conversely, the $c$ values for the third reaction step demonstrated significantly larger values during the reaction step, in comparison with those evaluated without incorporating the kinetic data in a stream of dry $N_2$ (Figure S43(c)). This result underscores the substantial effect of $p(H_2O)_{SG}$ on the third reaction step, which is characterized by a rapid increase and subsequent decrease in the reaction rate.

The apparent $E_{a,2}$ values for the second reaction step exhibited an initial escalation, as in the previous estimation (Figure S42(c)); however, approximately constant values were evaluated in the subsequent primary stage to the end of the reaction step (Figure 10(c)). Concerning the third reaction step, a slightly decreasing trend of the $E_{a,3}$ values was observed as the reaction progressed, in accordance with the previous estimation (Figure S43(c)). In both reaction steps, the $E_{a,i}$ values demonstrated a decline in comparison with the previous estimation that did not incorporate the kinetic data in a stream of dry $N_2$. This also led in a decline of the intrinsic $E_{a,i}$ values calculated according to eq. (17) (Figures 10(c) and 11(c)). The extended experimental master plots of the individual reaction steps demonstrated an analogous form with those evaluated in the previous kinetic analyses for the reactions in a stream of wet $N_2$ with varying $p(H_2O)_{ATM}$ values (Figures 10(d) and 11(d)). However, the $A_i$ values, determined by fitting the experimental master plots for the individual reaction steps using SB($m$, $n$, $p$), were found to be lower than those determined in the previous estimation. Consequently, the intrinsic $A_i$ values calculated according to eq. (18) also demonstrated a decline in both the reaction steps.

Table 3 enumerates the kinetic parameters that universally describe the kinetics of the second and third reaction steps of the thermal decomposition of $Ni(OH)_2$ across a range of $p(H_2O)_{ATM}$ values, including those under negligible $p(H_2O)_{ATM}$ conditions, determined by considering the effects of $p(H_2O)_{SG}$ and $p(H_2O)_{ATM}$. The intrinsic $E_{a,2}$ value was found to be marginally larger than the intrinsic $E_{a,3}$ value, while the intrinsic $A_2$ and $A_3$ values were comparable within the range of the standard error. The magnitude relationships between the intrinsic Arrhenius parameters of the second and third reaction steps are indicative of the second reaction step being more difficult kinetic process. Consequently, the sequence of the reaction steps is predicted to be regulated by a physico-geometrical constraint of the reaction. In addition, the $a = b$ value in AF indicated the larger value for the second reaction step, denoting the larger retardation effect of $p(H_2O)_{ATM}$. Therefore, the retardation of the primary thermal decomposition process of $Ni(OH)_2$ with increasing $p(H_2O)_{ATM}$ is interpreted to be controlled by the second reaction step.



**Table 3.** Apparent kinetic parameters for the second and third reaction steps of the thermal decomposition of $Ni(OH)_2$ in a stream of dry and wet $N_2$, determined by considering the effects of $p(H_2O)_{SG}$ and $p(H_2O)_{ATM}$ values, with the optimized $a = b$ and coefficients ($c$, $d$)[a], as well as the intrinsic Arrhenius parameters calculated according to eqs. (17) and (18)

| Reaction step, $i$ | $a = b$ | $E_{a,i}$ / kJ mol$^{-1}$, [b] | $\frac{(d\alpha_i/d\theta_i)}{h\left(p(H_2O),P_{eq}(T)\right)} = A_i f_i(\alpha_i)$ with $f_i(\alpha_i) = \alpha_i^{m_i}(1-\alpha_i)^{n_i}[-\ln(1-\alpha_i)]^{p_i}$ | | | | | Intrinsic Arrhenius parameters, [b] | |
|---|---|---|---|---|---|---|---|---|---|
| | | | $A_i$ / s$^{-1}$ | $m_i$ | $n_i$ | $p_i$ | R$^{2}$, [c] | $E_{a,i,int}$ / kJ mol$^{-1}$ | $A_{i,\,int}$ / s$^{-1}$ |
| 2 | 0.48 | 195.9 ± 1.1 | (6.10 ± 0.06) × 10$^{15}$ | −1.30 ± 0.18 | 1.36 ± 0.07 | 1.42 ± 0.17 | 0.9987 | 172.6 ± 1.1 | (9.52 ± 0.82) × 10$^{11}$ |
| 3 | 0.30 | 180.4 ± 2.0 | (2.48 ± 0.01) × 10$^{14}$ | 0.46 ± 0.02 | 0.97 ± 0.01 | 0.11 ± 0.02 | 0.9999 | 165.8 ± 2.0 | (1.83 ± 0.03) × 10$^{12}$ |

[a] Coefficient $c$ was optimized at individual $\alpha_i$ values, while $d$ was fixed to be unity.

[b] Averaged over $0.10 \le \alpha_i \le 0.90$.

[c] Determination coefficient of the nonlinear least-squares analysis.

The rate behaviors of each reaction step under isothermal conditions can be further assessed based on the extended experimental master plots or the SB($m_i$, $n_i$, $p_i$) functions, by considering the reaction sequence and the contributions of the second and third reaction steps. As illustrated in Figure 12, the extended experimental master plots are fitted using physicochemical and physico-geometrical kinetic model functions. The second reaction step was interpreted as the preparatory process within the primary thermal decomposition process of $Ni(OH)_2$, with a limited contribution $c_2/(c_2 + c_3) \approx 0.2$. The rate behavior of the second reaction step in a stream of dry $N_2$ was characterized by a linear deceleration following the initial short acceleration stage (Figure S19(a)), which was interpreted as exhibiting the characteristics of the F1 model. One potential explanation for this phenomenon is that it is due to the consumption of the reactive sites on the surfaces of the $Ni(OH)_2$ agglomerates. The extended experimental master plot, which universally describe the rate behavior across a range of $p(H_2O)_{EF}$ values, exhibited the deceleration behavior with a convex shape (Figure 12(a)), following a short acceleration stage. In accordance with the anticipated physico-geometrical reaction scheme of the consumption of the active sites in the surface, the rate behavior was described by the JAM($m$) model with $m = 1.31 \pm 0.01$.

The extended experimental master plot of the third reaction step (Figure 12(b)) exhibited a limited variation from that of the conventional experimental master plot for the reactions in a stream of dry $N_2$ (Figure S19(b)), which was characterized by the swift acceleration and deceleration with the contribution of $c_3/(c_2 + c_3) \approx 0.8$. The rate behavior of the third reaction step in a stream of dry $N_2$ was described by JMA(2.39) or ePT(0.52, 0.70) with equivalent statistical significance (Figure S19(b)), while ePT($m$, $n$) with $m = 0.57 \pm 0.01$ and $n = 0.93 \pm 0.01$ yielded better fit to the extended experimental master plot than that with JMA($m$) with $m = 1.91 \pm 0.01$. However, the random nucleation and the expansion of the volume of the product phase in the $Ni(OH)_2$ matrix, as described by the JMA($m$) model, is one possible physico-geometrical model for describing the autocatalytic behavior of the third reaction step.



View Article Online
DOI: 10.1039/D6CP00975A



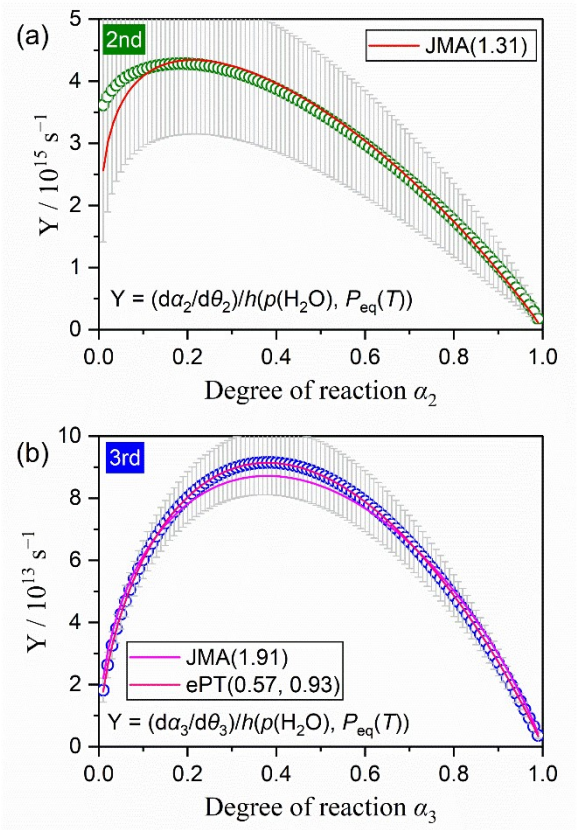


**Figure 12.** Analyses of the extended experimental master plots of the individual reaction steps using physicochemical and physico-geometrical kinetic model functions: (a) second and (b) third reaction steps.

## 4. Conclusions

The thermal decomposition of $Ni(OH)_2$ exhibiting three-step mass loss process was interpreted as comprising the sequential processes of the dehydration of absorbed or included water molecules in the $Ni(OH)_2$ agglomerate, followed by the primary step of the thermal decomposition of $Ni(OH)_2$ and subsequent evolution of trapped water accompanied by the crystal growth of NiO. The primary reaction step was identified as the actual thermal decomposition process of $Ni(OH)_2$ to form NiO, accompanied by a dramatic increase in the specific surface area. A kinetic modeling of a four-step kinetic process was proposed based on the formal kinetic analysis and subsequent MDA and KDA procedures as applied to the thermal decomposition under various temperature variation conditions in a stream of dry $N_2$. In this model, the primary mass loss process was considered as comprising partially overlapping two-step process. The initial step of the primary reaction process was considered as the preparatory process with a small contribution occurring by the consumption of reactive sites on the surfaces of $Ni(OH)_2$ agglomerates. The subsequent step exhibited an autocatalytic rate behavior, which was interpreted as regulated by the nucleation and expansion of the solid product phase in the $Ni(OH)_2$ matrix. A distinctive retardation effect of $p(H_2O)_{ATM}$ on the primary reaction process of the thermal decomposition of $Ni(OH)_2$ was evidenced by a systematic TG measurements in a stream of wet $N_2$ with controlled $p(H_2O)_{ATM}$. The effect of $p(H_2O)_{ATM}$ on the individual reaction steps in the primary reaction process was parameterized in the context of an extended kinetic equation incorporated an AF describing universally the kinetic behavior as a function of $T$, $\alpha$, $p(H_2O)_{ATM}$. The extended kinetic description was able to further extend by incorporating the effect of $p(H_2O)_{SG}$, providing a finding of the

significant effect of $p(H_2O)_{SG}$ during the latter reaction step in the primary reaction process of the thermal decomposition of $Ni(OH)_2$. After considerable efforts, the universal kinetic description of the individual reaction steps was finally achieved, encompassing all kinetic behavior, including those traced in a stream of dry $N_2$ and wet $N_2$ with varying $p(H_2O)_{ATM}$. The apparent kinetic parameters determined through the extended kinetic approach to the individual reaction steps can be utilized to simulate the reaction behavior at a selected temperature and $p(H_2O)_{ATM}$ values. The final kinetic results indicated that the initial reaction step in the primary reaction process is regulative of the kinetics of the primary thermal decomposition process. In addition, the effect of $p(H_2O)_{ATM}$ is more distinguishable in the initial reaction step. These novel kinetic findings concerning the primary thermal decomposition process of $Ni(OH)_2$ indicate that controlling the initial reaction step can alter the overall kinetics and the reaction conditions of NiO formation. This may be achieved by controlling the properties of $Ni(OH)_2$ precursors and the reaction conditions of its thermal decomposition process.

## Conflicts of Interest

There are no conflicts of interest to declare.

## Electronic Supplementary Information

Electronic supplementary information (ESI) is available: S1. Sample preparation and characterization (Figures S1–S3), S2. Thermal behavior (Figures S4–S6), S3. Thermal decomposition in a stream of dry $N_2$ (Figures S7–S19; Tables S1–S4), S4. Thermal decomposition in a stream of wet $N_2$ with various atmospheric water vapor pressures (Figures S20–S41; Tables S5–S9), S5. Universal kinetic description considering atmospheric and self-generated water vapor pressures (Figures S42 and S43; Table S10).

## Corresponding Author

*Tel./fax: +81-82-424-7092. E-mail: nkoga@hiroshima-u.ac.jp

## ORCID

Nobuyoshi Koga: 0000-0002-1839-8163

Mito Hotta: 0009-0003-0104-6190

## Acknowledgements

The present work was supported by JSPS KAKENHI Grant Numbers 23K22282, 24K05970, 24K21457, and 25KJ1876.

## References

1. D. S. Hall, D. J. Lockwood, C. Bock and B. R. MacDougall, *Proc. Math. Phys. Eng. Sci.*, 2015, **471**, 20140792.
2. A. Azens, *Solid State Ionics*, 1998, **113-115**, 449-456.
3. I. Hotovy, J. Huran, L. Spiess, S. Hascik and V. Rehacek, *Sens. Actuators, B*, 1999, **57**, 147-152.
4. K. Fominykh, J. M. Feckl, J. Sicklinger, M. Döblinger, S. Böcklein, J. Ziegler, L. Peter, J. Rathousky, E. W. Scheidt, T. Bein and D. Fattakhova-Rohlfing, *Adv. Funct. Mater.*, 2014, **24**, 3123-3129.

5. R. Kumar, R. K. Singh, R. Savu, P. K. Dubey, P. Kumar and S. A. Moshkalev, *RSC Adv.*, 2016, **6**, 26612-26620.
6. M. A. Nasseri, F. Ahrari and B. Zakerinasab, *Appl. Organomet. Chem.*, 2016, **30**, 978-984.
7. D.-L. Sun, B.-W. Zhao, J.-B. Liu, H. Wang and H. Yan, *Ionics*, 2017, **23**, 1509-1515.
8. Y. Abdelbaki, A. de Arriba, R. Issaadi, R. Sánchez-Tovar, B. Solsona and J. M. López Nieto, *Fuel Process. Technol.*, 2022, **229**.
9. M. Imran Din and A. Rani, *Int. J. Anal. Chem.*, 2016, **2016**, 1-14.
10. J. Mou, Y. Ren, J. Wang, C. Wang, Y. Zou, K. Lou, Z. Zheng and D. Zhang, *Microfluid. Nanofluid.*, 2022, **26**, 25.
11. S. S. Narender, V. V. S. Varma, C. S. Srikar, J. Ruchitha, P. A. Varma and B. V. S. Praveen, *Chem. Eng. Technol.*, 2022, **45**, 397-409.
12. W. Ahmad and A. Rawat, *Nat., Environ. Pollut. Technol.*, 2023, **22**, 1353-1362.
13. K. Arima, Y. Aoki, M. Hotta and N. Koga, *Ind. Eng. Chem. Res.*, 2025, **64**, 7298-7312.
14. I. F. Hazell and R. J. Irving, *J. Chem. Soc. A*, 1966, 669-673.
15. J. M. Fernández Rodfríguez, J. Morales and J. L. Tirado, *J. Mater. Sci.*, 1986, **21**, 3668-3672.
16. Z.-H. Liang, Y.-J. Zhu and X.-L. Hu, *J. Phys. Chem. B*, 2004, **108**, 3488-3491.
17. X. Zhang, W. Shi, J. Zhu, W. Zhao, J. Ma, S. Mhaisalkar, T. L. Maria, Y. Yang, H. Zhang, H. H. Hng and Q. Yan, *Nano Res.*, 2010, **3**, 643-652.
18. V. Logvinenko, V. Bakovets and L. Trushnikova, *J. Therm. Anal. Calorim.*, 2011, **107**, 983-987.
19. A. Tang, X. Li, Z. Zhou, J. Ouyang and H. Yang, *J. Alloys Compd.*, 2014, **600**, 204-209.
20. R. Yahyaoui and K. Nahdi, *Inorg. Chem.:Indian J.*, 2016, **11**, 1-9.
21. N. M. Zali, T.-F. Choo, N. U. Saidin and K.-Y. Kok, *AIP Conf. Proc.* , 2024, **2925**, 020001.
22. R. M. Gabr, A. N. El-Naimi and M. G. Al-Thani, *Thermochim. Acta*, 1992, **197**, 307-318.
23. C. S. Carney, R. E. Chinn, Ö. N. Doğan and M. C. Gao, *J. Alloys Compd.*, 2015, **644**, 968-974.
24. O. T. Sørensen and J. Rouquerol, *Sample Controlled Thermal Analysis*, Kluwer, Dordrecht, 2003.
25. S. Vyazovkin, A. K. Burnham, L. Favergeon, N. Koga, E. Moukhina, L. A. Perez-Maqueda and N. Sbirrazzuoli, *Thermochim. Acta*, 2020, **689**, 178597.
26. N. Koga, S. Vyazovkin, A. K. Burnham, L. Favergeon, N. V. Muravyev, L. A. Pérez-Maqueda, C. Saggese and P. E. Sánchez-Jiménez, *Thermochim. Acta*, 2023, **719**, 179384.
27. S. Vyazovkin, *Int. Rev. Phys. Chem.*, 2020, **39**, 35-66.
28. S. Kodani, S. Iwasaki, L. Favergeon and N. Koga, *Phys. Chem. Chem. Phys.*, 2020, **22**, 13637-13649.
29. N. Koga, L. Favergeon and S. Kodani, *Phys. Chem. Chem. Phys.*, 2019, **21**, 11615-11632.
30. M. Fukuda, L. Favergeon and N. Koga, *J. Phys. Chem. C*, 2019, **123**, 20903-20915.
31. S. Fukunaga, Y. Zushi, M. Hotta and N. Koga, *Phys. Chem. Chem. Phys.*, 2025, **27**, 3384-3400.
32. M. Hotta, Y. Zushi, S. Iwasaki, S. Fukunaga and N. Koga, *Phys. Chem. Chem. Phys.*, 2023, **25**, 27114-27130.
33. M. Hotta, L. Favergeon and N. Koga, *J. Phys. Chem. C*, 2023, **127**, 13065-13080.
34. Y. Zushi, S. Iwasaki and N. Koga, *Phys. Chem. Chem. Phys.*, 2022, **24**, 29827-29840.
35. Y. Yamamoto, L. Favergeon and N. Koga, *J. Phys. Chem. C*, 2020, **124**, 11960-11976.
36. S. Fukunaga, M. Hotta and N. Koga, *J. Phys. Chem. C*, 2026, DOI: 10.1021/acs.jpcc.5c07824.
37. M. Hotta, T. Tone, L. Favergeon and N. Koga, *J. Phys. Chem. C*, 2022, **126**, 7880-7895.
38. N. Koga, Y. Sakai, M. Fukuda, D. Hara, Y. Tanaka and L. Favergeon, *J. Phys. Chem. C*, 2021, **125**, 1384-1402.
39. Y. Kodani, K. Arima, S. Fukunaga, M. Hotta and N. Koga, *J. Phys. Chem. C*, 2025, **129**, 20207-20222.



40. M. Hotta and N. Koga, *Netsu Sokutei*, 2025, **52**, 2-10.
41. M. Hotta and N. Koga, *Thermochim. Acta*, 2024, **733**, 179699.
42. T. N. Ramesh, R. S. Jayashree and P. Vishnu Kamath, *J. Electrochem. Soc.*, 2003, **150**, A520-524.
43. T. N. Ramesh, *J. Phys. Chem. B*, 2009, **113**, 13014-13017.
44. O. T. Sørensen, *J. Therm. Anal.*, 1978, **13**, 429-437.
45. A. Szytula, A. Murasik and M. Balanda, *Phys. Status Solidi B*, 1971, **43**, 125-128.
46. J. Tientong, S. Garcia, C. R. Thurber and T. D. Golden, *J. Nanotechnol.*, 2014, **2014**, 1-6.
47. K. Lawson, S. P. Wallbridge, A. E. Catling, C. A. Kirk and S. E. Dann, *J. Mater. Chem. A*, 2023, **11**, 789-799.
48. E. Konysheva, E. Suard and J. T. S. Irvine, *Chem. Mater.*, 2009, **21**, 5307-5318.
49. N. Koga and H. Tanaka, *J. Therm. Anal.*, 1993, **40**, 1173-1179.
50. S. Iwasaki, Y. Zushi and N. Koga, *Phys. Chem. Chem. Phys.*, 2021, **23**, 22972-22983.
51. Y. Zushi, S. Iwasaki and N. Koga, *Phys. Chem. Chem. Phys.*, 2022, **24**, 15736-15748.
52. H. Tanaka and N. Koga, *J. Therm. Ana.l*, 1990, **36**, 2601-2610.
53. S. Vyazovkin, K. Chrissafis, M. L. Di Lorenzo, N. Koga, M. Pijolat, B. Roduit, N. Sbirrazzuoli and J. J. Suñol, *Thermochim. Acta*, 2014, **590**, 1-23.
54. H. L. Friedman, *J. Polym. Sci., ,Part C*, 1964, **6**, 183-195.
55. N. Koga, Y. Goshi, S. Yamada and L. A. Pérez-Maqueda, *J. Therm. Anal. Calorim.*, 2013, **111**, 1463-1474.
56. N. Koga, in *Handbook of Thermal Analysis and Calorimetry*, eds. S. Vyazovkin, N. Koga and C. Schick, Elsevier, Amsterdam, 2nd edn., 2018, vol. 6, ch. 6, pp. 213-251.
57. A. Perejón, P. E. Sánchez-Jiménez, J. M. Criado and L. A. Pérez-Maqueda, *J. Phys. Chem. B*, 2011, **115**, 1780-1791.
58. R. Svoboda and J. Málek, *J. Therm. Anal. Calorim.*, 2013, **111**, 1045-1056.
59. T. Ozawa, *Bull. Chem. Soc. Jpn.*, 1965, **38**, 1881-1886.
60. T. Ozawa, *Thermochim. Acta*, 1986, **100**, 109-118.
61. J. Málek, *Thermochim. Acta*, 1992, **200**, 257-269.
62. N. Koga, *Thermochim. Acta*, 1995, **258**, 145-159.
63. F. J. Gotor, J. M. Criado, J. Malek and N. Koga, *J. Phys. Chem. A*, 2000, **104**, 10777-10782.
64. J. M. Criado, L. A. Perez-Maqueda, F. J. Gotor, J. Malek and N. Koga, *J. Therm. Anal. Calorim.*, 2003, **72**, 901-906.
65. P. E. Sánchez-Jiménez, A. Perejón, J. M. Criado, M. J. Diánez and L. A. Pérez-Maqueda, *Polymer*, 2010, **51**, 3998-4007.
66. J. Šesták and G. Berggren, *Thermochim. Acta*, 1971, **3**, 1-12.
67. J. Šesták, *J. Therm. Anal.*, 1990, **36**, 1997-2007.
68. J. Šesták, *J. Therm. Anal. Calorim.*, 2011, **110**, 5-16.
69. E. G. Prout and F. C. Tompkins, *Trans. Faraday Soc.*, 1944, **40**, 488-498.
70. W. A. Johnson and K. F. Mehl, *Trans. Am. Inst. Min. Metall. Eng.*, 1939, **135**, 416-458.
71. M. Avrami, *J Chem Phys*, 1939, **7**, 1103-1112.
72. M. Avrami, *J Chem Phys*, 1940, **8**, 212-223.
73. M. Avrami, *J Chem Phys*, 1941, **9**, 177-184.
74. B. V. Erofeyev, *CR Acad. Sci. URSS*, 1946, **52**, 511-514.
75. N. N. Kolmogorov, *Bull. Acad. Sci. USSR, Math. Ser. 1*, 1937, 355-359.



76. A. K. Galwey and W. J. Hood, *J. Phys. Chem.*, 1979, **83**, 1810-1815.
77. T. Wada, M. Nakano and N. Koga, *J. Phys. Chem. A*, 2015, **119**, 9749-9760.
78. K. L. Mampel, *Z. Phys. Chem. Abt. A*, 1940, **187**, 43-57
79. K. L. Mampel, *Z. Phys. Chem. Abt. A*, 1940, **187**, 234-249.
80. H. Ogasawara and N. Koga, *J. Phys. Chem. A*, 2014, **118**, 2401-2412.
81. L. Favergeon, M. Pijolat and M. Soustelle, *Thermochim. Acta*, 2017, **654**, 18-27.
82. D. D. Wagman, W. H. Evans, V. B. Parker, R. H. Schumm, I. Halow, S. M. Bailey, K. L. Churney and R. L. Nuttall, *The NBS Tables of Chemical Thermodynamic Properties. Selected Values for Inorganic and C1 and C2 Organic Substances in SI Units*, American Chemical Society, Washington, DC, 1982.

View Article Online
DOI: 10.1039/D6CP00975A



## Data Availability Statement

View Article Online
DOI: 10.1039/D6CP00975A

Data will be made available on request.